A New Image Registration Technique With Free Boundary Constraints: Application To Mammography

Frédéric J.P. RICHARD * and Laurent D. COHEN **

In this paper, a new image-matching mathematical model is presented with its application to mammogram registration. In a variational framework, an energy minimization problem is formulated and a multigrid resolution algorithm is designed. The model focuses on the matching of regions of interest. It also combines several constraints which are both intensity and segmentation based. A new feature of our model is combining region matching and segmentation by formulation of the energy minimization problem with free boundary conditions. Moreover, the energy has a new registration constraint. The performances of the new model and an equivalent model with fixed boundary conditions are compared on simulated mammogram pairs. It is shown that the model with free boundary is more robust to initialization inaccuracies than the one with fixed boundary conditions. Both models are applied to several real bilateral mammogram pairs. The model ability to compensate significantly for some normal differences between mammograms is illustrated. Results suggest that the new model could enable some improvements of mammogram comparisons and tumor detection system performances.

Key words: Energy Minimization, Variational Method, Partial Derivative Equations, Finite Elements, Multigrid, Image Matching, Image Registration, Deformable Model, Mammography

---

*University Paris 5 - René Descartes, MAP5, FRE CNRS 2428, UFR mathématiques/informatique, 45, rue des Saints Pères, 75 270 Paris Cedex 06, France. e-mail: richard@math-info.univ-paris5.fr

**University Paris 9 - Dauphine, CEREMADE, UMR CNRS 7534, Place du maréchal de Lattre de Tassigny, 75775 Paris cedex 16, France. e-mail: cohen@ceremade.dauphine.fr

1. Introduction

Image Registration has been an active topic of research for over a decade. Its most famous medical applications are related to brain imagery [57]. For instance, Image Registration is used in computational anatomy as tool for analyzing brain structures by adapting an anatomical template to individual anatomies [11, 12, 20, 22]. However, Image Registration is a general problem which arises whenever several images are to be compared or data from several images to be fused.

As can be seen though the complete survey in [38], a lot of work has been done in Image Registration since the early 80's. The registration techniques are usually divided into two groups. Techniques of the first kind use features such as points and curves to match the images [7]. Such techniques require that features be extracted prior to registration. Techniques of the second kind use image gray level values. Among these intensity-based techniques, some are non-rigid and based on the squared intensity difference minimization criteria [1, 3, 8, 10, 12, 18, 20, 37, 44, 64].

In [45, 47], F. Richard and C. Graffigne described an approach for combining feature based and intensity based registration constraints in a same mathematical model. The approach focuses on the mapping of regions of interest rather than the whole image matching. The model consists of minimizing an intensity-based energy with some fixed boundary conditions (Dirichlet) which are derived from contours of regions of interest (see section 2.2). In [45, 47], the model was applied to mammograms. It was shown that thanks to the combined constraints the computation time and the mammogram registration accuracy improved. However, model performances depend on the quality of some preprocessing steps (segmentation of image regions of interest and matching of contours). Indeed, since boundary conditions are fixed, preprocessing inaccuracies cannot be corrected during the matching process. Hence these inaccuracies may decrease matching performances. Besides, Dirichlet boundary conditions constrain too strongly the problem and may sometimes disrupt breast registrations near contours.

In this paper, our main contribution is the design of a new mathematical model which fixes the drawbacks described above by combining region matching and segmentation. As in [45, 47], the model enables the matching of regions of interest. But, contrarily to the model in [45, 47], the minimization problem is defined with free boundary conditions allowing to make evolution in the segmentation of the region of interest. Consequently, the boundary conditions are relaxed and it becomes possible to compensate for preprocessing inaccuracies during the matching process. Furthermore, some constraints are proposed in order to compensate efficiently for preprocessing inaccuracies and increase the model robustness.

The approach we propose in this paper is related to the ones described in [58, 65]. In [58, 65], a unified variational framework which enables to interleave segmentation and registration is also designed. However, our approach differs significantly from the ones in [58, 65]. The model in [65] deals only with rigid registration and does only have feature-based registration constraints. The model in [58] deals with nonrigid registration but does not take into account regions of interest for mapping one image onto the other.

In this paper, the new registration model is applied to bilateral mammogram pairs (mammograms of left and right breasts of same women). The context of this application is related to the design of automatic tumor detection systems for the CAD (Computer Aided Diagnosis). It will be described in section 4.1. Mammogram registration is a challenging problem. Several

mammogram registration techniques are only based on breast contours [29, 36, 40]. Thus, these techniques cannot succeed in registering correctly breast interiors. In [39, 41, 48, 50, 52], some authors attempted to register breast interiors using the Bookstein warping technique with internal control points [7]. Following such an approach, the main problem is to extract from both mammograms points which are anatomically significant, sufficiently numerous and distributed over the images and to match some extracted points of both images. The difficulty is to design point extraction and matching techniques which are robust to factors which can change image aspects (e.g. the breast compression level).

The registration approach proposed in this paper departs from the ones in [39, 41, 48, 50, 52]. First of all, the new model is not based on internal control points. Hence, the difficulty mentioned above is avoided. Secondly, thanks to intensity-based registration constraints, the model can register breast interiors more accurately than models based on internal control points. Finally, the model takes into account regions of interest (i.e. breasts) and combines efficiently intensity-based constraints with contour-based constraints in an unified mathematical framework.

The new image-matching approach and its mathematical formulation is presented in section 2. In section 3, a multigrid algorithm is designed for the numerical resolution of the problem. Illustrations and validations of the algorithm application to mammograms are given in section 4.

2. Models

In this section, three different image-matching problems are formulated. In section 2.1, the formulation of the usual intensity-based problem is reminded. Sections 2.2 and 2.3 are both devoted to the matching of regions of interest. In section 2.2, we recall the formulation of our previous model [45, 47]. In section 2.3, the new model is presented.

2.1. The Classical Model

The classical variational framework for Image Matching is the following [1, 3, 12, 37, 44, 64]. Let Ω be a connected and open set of $\mathbb{R}^2$ and I^0 and I^1 be two images defined on Ω using interpolation. Let us denote by $\overline{\Omega}$ the set which is the closure of Ω (with respect to the euclidean norm of $\mathbb{R}^2$) and contains the set Ω and its boundary. Let $\mathcal{W}_1$ be a space composed of smooth functions mapping $\overline{\Omega}$ onto itself. Let us denote by I^0_ϕ the geometric deformation of I^0 that is induced by the element ϕ of $\mathcal{W}_1$:

$$\forall\, x \in \Omega,\ \ I^0_\phi(x) = I^0 \circ \phi(x).$$

Matching I^0 and I^1 consists of finding an element ϕ which is such that the deformed image I^0_ϕ is "similar" to I^1. This is expressed in terms of an inverse problem [1, 3, 12, 37, 44, 64]:
Model 1 *Find an element of $\mathcal{W}_1$ which minimizes an energy J_1 of the following form:*

$$J_1(u) = \frac{1}{2}\, A_\Omega(u,u) + \frac{\gamma_1}{2} |I^0_\phi - I^1|^2_\Omega, \tag{1}$$

with some conditions on the boundary of Ω. In this energy definition, the parameter γ_1 belongs to $\mathbb{R}^+$. The variable u belongs to $\mathcal{W}_1$. It is equal to $\phi - \mathrm{Id}$, where Id is the identity map of $\mathcal{W}_1$ (i.e. $\forall\, x \in \overline{\Omega}, \mathrm{Id}(x) = x$) . It is the displacement field associated to the deformation ϕ. The

function $|\cdot|_\Omega$ *denotes the usual quadratic norm on* $L^2(\overline{\Omega};\mathbb{R})$*, i.e.:*

$$|I|^2_\Omega = \int_\Omega I^2(x)dx.$$

The energy in equation (1) is composed of two terms. The second term, which is weighted by the parameter γ_1, depends on the images. The more similar the images I^0_ϕ and I^1 are, the lower this term is. It introduces an intensity-based matching constraint into the model. The first term is a smoothing term which ensures that the problem is well-posed and that solutions are non-degenerate solutions. Its design is usually based on a strain energy of the continuum mechanics. Inspired by the theory of linearized Elasticity [14], we define the strain energy as in [45]

$$A_\Omega(u,v) = \langle Lu, v\rangle_\Omega = \int_\Omega Lu(x)\cdot v(x)\,dx, \tag{2}$$

for any $u, v \in \mathcal{W}_1$, where $\langle\cdot,\cdot\rangle_\Omega$ is the usual scalar product on $L^2(\overline{\Omega};\mathbb{R}^2)$ and L is the following operator [1]

$$Lu = -\mathrm{div}\{\lambda\,\mathrm{tr}(\mathbf{e}(u))\mathrm{Id}_M + 2\,\mu\,\mathbf{e}(u)\}. \tag{3}$$

where λ and μ are two positive values called the Lame coefficients, Id_M is the identical matrix of size 2×2 and $\mathbf{e}(u)$ is the linearized strain tensor $1/2(\nabla u^T + \nabla u)$. The elastic smoothing term is suitable for the registration of images which do not have large geometric disparities. In the mammogram application, it ensures that problem solutions are homeomorphisms. An application of model 1 to a mammogram pair is shown in figure 1; this example will be commented further in section 4.

2.2. Region-Matching With Fixed Boundary Conditions

Unlike the previous model, the model presented in this section focuses on regions of interest. The framework is the following. Let us assume that the images I^0 and I^1 have single regions of interest which are respectively located on the connected and open subsets Ω_0 and Ω_1 of Ω. This means that for each image, the domain can be segmented in one region of interest (Ω_0 or Ω_1) and the background ($\Omega-\Omega_0$ or $\Omega-\Omega_1$). Let us denote by $\partial\Omega_0$ and $\partial\Omega_1$ the boundaries of Ω_0 and Ω_1, respectively. We assume that the contours $\partial\Omega_0$ and $\partial\Omega_1$ were previously extracted and matched. Let ϕ_0 (or $\mathrm{Id}+u_0$) be a function defined on Ω_1 and mapping the coordinates of $\partial\Omega_1$ onto those of $\partial\Omega_0$. In order to focus on the regions of interest, the minimization problem is not defined on $\mathcal{W}_1$ (see section 2.1) but on a space $\mathcal{W}_2$ which is composed of smooth functions mapping $\overline{\Omega_1}$ onto $\overline{\Omega_0}$. The inverse problem is stated as follows [45, 47]:

Model 2 *Find an element of* $\mathcal{W}_2$ *which minimizes an energy* J_2 *of the following form:*

$$J_2(u) = \frac{1}{2}\,A_{\Omega_1}(u,u) + \frac{\gamma_1}{2}|I^0_\phi - I^1|^2_{\Omega_1}, \tag{4}$$

[1] If M is a 2×2-matrix, then $\mathrm{tr}(M)$ is equal to $M_{11}+M_{22}$. If m is a smooth function mapping Ω into the 2×2-matrix set, then the value of $\mathrm{div}\{m\}$ at a point x of Ω is a bidimensional vector having the i^{th} component equal to $\partial_{x_1} m(x)_{i1} + \partial_{x_2} m(x)_{i2}$.

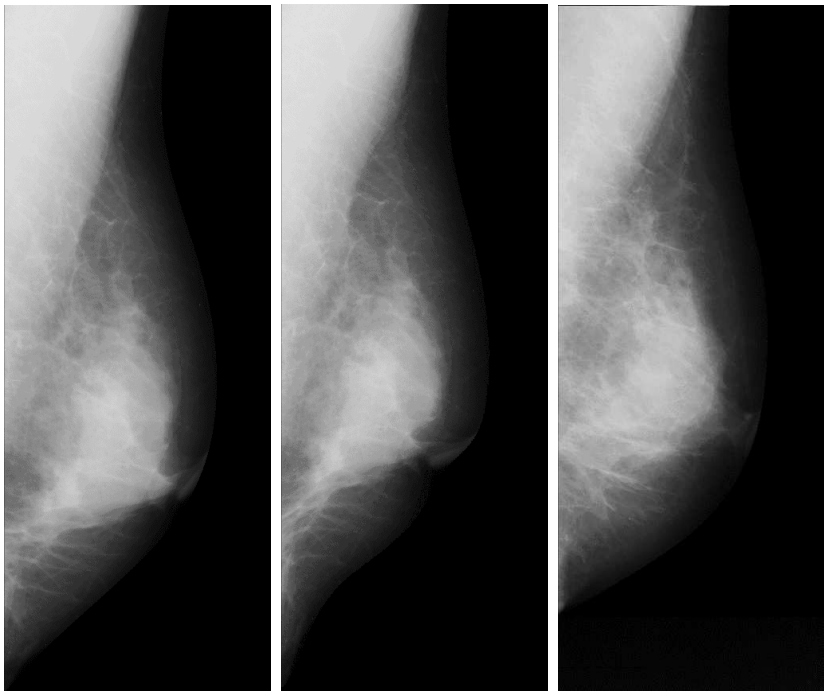

(a) (b) (c)

Figure 1. (a) The source image I^0, (b) the geometric deformation I^0_ϕ of I^0 after the application of model 1, (c) the target image I^1. Images (a) and (c) are mammograms of left and right breasts (source: MIAS database [55]).

with the following non-homogeneous Dirichlet boundary conditions:

$$\forall\, x \in \partial\,\Omega_1,\ u(x) = u_0(x) = \phi_0(x) - x.$$

The terms of energy J_2 have the same definitions and play the same roles as those of energy J_1 in model 1. However, they are not defined on the whole domain Ω but only on the region of interest Ω_1. Besides, the boundary conditions are specific to the regions of interest and based on a known matching of their contours. An application of model 2 is shown on figure 5.

2.3. Region-Matching With Free Boundary Conditions

The model presented in this section focuses on the regions of interest. But, unlike the previous model, the problem is defined with free boundary conditions. Hence, the problem is not defined on $\mathcal{W}_2$ (see section 2.2) but on a space $\mathcal{W}_3$ which is composed of smooth functions mapping $\overline{\Omega_1}$ onto $\mathbb{R}^2$. The inverse problem is defined as follows [46]:

Model 3 (first formulation). *Find an element of $\mathcal{W}_3$ which minimizes an energy $\tilde{J}_3$ of the following form:*

$$\tilde{J}_3(u) = \frac{1}{2}\, A_{\Omega_1}(u,u) + \gamma_1\, \frac{1}{2} |I^0_\phi - I^1|^2_{\Omega_1} + \gamma_2 \int\limits_{\Omega - \phi(\Omega_1)} S((I^0(x))^2) dx, \tag{5}$$

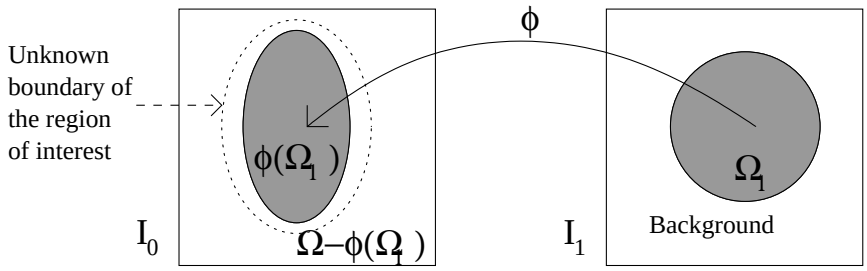

Figure 2. A schematic picture of region-matching with free boundary conditions.

with free boundary conditions on $\partial\Omega_1$.
In the energy definition, the weighting parameters γ_1 and γ_2 both belong to $\mathbb{R}^+$. As in models 1 and 2, the energy has a matching and a regularity term. It has also a term which depends on image I^0. This term is defined on a region $\Omega - \phi(\Omega_1)$ which is expected to be the background of I^0 (see figure 2). It is a term which constrains ϕ to map points of Ω_1 out of the background domain of I^0. For reasons that will appear next, it will be referred as the segmentation term. An application of model 3 is shown in figure 5.

Design of S**.** Assume that the image I^0 can be robustly segmented using a threshold; that is to say there exists a value η such that $(I^0(x))^2 < \eta$ if and only if x belongs to the background of the image I^0. Then, S can be defined as a smooth distribution function approximating on a bounded interval the function that is equal to 0 on $(-\infty, \eta[$ and 1 on $[\eta, +\infty)$. The value of S at a point r of $\mathbb{R}$ may be interpreted as the conditional probability for a pixel x not to be on the image background knowing that $(I^0(x))^2$ is equal to r. In the case where the segmentation threshold is not accurate, the design of S can be based on an empirical estimation of these probabilities. For instance, in the mammogram application, these probabilities are estimated using an image I^1 for which segmentation is known. The function S is a smoothed version of the histogram of the image $(I^1)^2$ evaluated over the domain Ω_1. The typical shape of the estimated functions S is shown in figure 3.

Segmentation of I^0**.** Contrarily to model 2, a preliminary segmentation of the region of interest in I^0 is not needed for the problem formulation. A segmentation of I^0 is obtained after the problem resolution: the contour is given by the image $\phi(\partial\Omega_1)$ of $\partial\Omega_1$ by a function ϕ which minimizes the energy. Let us also remark that the unknown $\phi(\partial\Omega_1)$ is a parametrized curve and that, from the point of view of this unknown, model 3 is closely related to active contour models [15, 16, 17, 30].

An equivalent problem. Assuming some regularity conditions (the elements ϕ of $\mathcal{W}_3$ belong to the Sobolev hilbertian space[2] $H^1(\overline{\Omega_1}; \mathbb{R}^2)$ [14] and are such that $\det(\nabla\,\phi) > 0$ on Ω_1), it can be seen that

[2] In the definition of the Sobolev space, it is assumed that the domain boundary $\partial\Omega_1$ is continuous. Thanks to a contour smoothing, this assumption is true in practice; see more details in section 4.2.

$$\int\limits_{\Omega-\phi(\Omega_1)} S((I^0(x))^2)dx = \int\limits_{\Omega} S((I^0(x))^2)dx - \int\limits_{\Omega_1} S((I^0_\phi(x))^2)\,\det(\nabla\phi)\,dx, \tag{6}$$

where the real value $\det(\nabla\phi)$ is the Jacobian of the function ϕ. Thus, since the first term on the right does not depend on ϕ, the previous minimization problem can be restated in the following equivalent way:

Model 3 (equivalent formulation) *Find an element of $\mathcal{W}_3$ which minimizes an energy J_3 which is of the following form:*

$$J_3(u) = \frac{1}{2}\,A_{\Omega_1}(u,u) + \frac{\gamma_1}{2}|I^0_\phi - I^1|^2_{\Omega_1} - \gamma_2 \int\limits_{\Omega_1} S((I^0_\phi(x))^2)\,\det(\nabla\phi)\,dx, \tag{7}$$

with free boundary conditions on $\partial\Omega_1$.

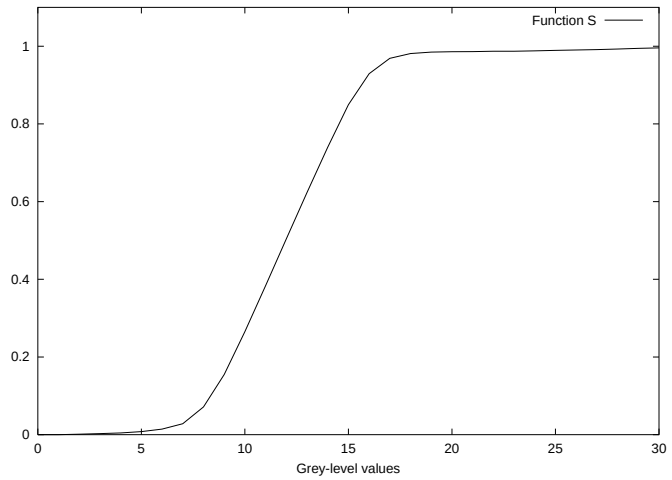

Figure 3. Typical shape of estimated functions S (model 3).

3. Numerical Solution

In this section, a gradient descent algorithm is designed for the numerical resolution of the problem of model 3. In section 3.1, the energy is derived and the algorithm is expressed in terms of a dynamic system. In section 3.2, we propose a spatial discretization of the dynamic system using the Galerkin method. In section 3.3, an initialization method is described. In section 3.4, a multigrid implementation of the algorithm is designed.

3.1. Gradient Descent Algorithm

The Frechet derivative of the energy J_3 (equation (7)) at a point u of $\mathcal{W}_3$ is as follows: for all v in $\mathcal{W}_3$

$$dJ_{3|_u}(v) = A_{\Omega_1}(u\ ,\ v) + \gamma_1\langle (I^0_\phi - I^1)\,\nabla I^0_\phi\ ,\ v\rangle_{\Omega_1} \tag{8}$$

$$-2\gamma_2 \int_{\Omega_1} \det(\nabla\phi) S'((I^0_\phi)^2) \nabla I^0_\phi \cdot v dx - \gamma_2 \int_{\Omega_1} S((I^0_\phi)^2) \mathrm{tr}(\mathrm{cof}(\nabla\phi)^T \cdot \nabla v)\, dx,$$

where $\mathrm{cof}(M)$ is the cofactor matrix of a matrix M ($\mathrm{cof}(M) = \det(M) M^{-T}$). Moreover, by a Green formula [14],

$$\int_{\Omega_1} S((I^0_\phi)^2)\ \mathrm{tr}(\mathrm{cof}(\nabla\phi)^T \cdot \nabla v)\, dx = -\int_{\Omega_1} \mathrm{div}\{S((I^0_\phi)^2)\ \mathrm{cof}(\nabla\phi)^T\} \cdot v\, dx. \tag{9}$$

Recall that the gradient ∇J of an energy J at a point u with respect to an inner product $\langle \cdot, \cdot \rangle$ is given by the element ∇J_u which is such that, for all v,

$$\langle \nabla J_u, v \rangle = dJ_{|u}(v)$$

Thus, from equations (8) and (9), it comes that the gradient of energy J_3 with respect to the inner product $A_{\Omega_1}(\cdot, \cdot)$ is

$$\nabla J_{3u} = u - L^{-1}\, F(\phi(t)), \tag{10}$$

where L is the operator defined by equation (3) and F is the following mapping:

$$\begin{aligned} F(\phi) = & -\gamma_1\, (I^0_\phi - I^1)\, \nabla I^0_\phi \\ & +2\, \gamma_2\ \det(\nabla\phi)\ S'((I^0_\phi)^2)\ \nabla I^0_\phi -\ \gamma_2\ \mathrm{div}\{S((I^0_\phi)^2)\ \mathrm{cof}(\nabla\phi)^T\}. \end{aligned} \tag{11}$$

Thus, the gradient descent of energy J_3 can be expressed in terms of the following dynamic system:

Algorithm 1 (gradient descent) *The gradient descent is*

$$\forall\ t < 0,\ \ \frac{du}{dt}(t) = -u(t) + \delta(t) \quad \text{and} \quad u(0) = M_0, \tag{12}$$

where the initial deformation M_0 will be defined in section 3.3, and at each time t, $\delta(t)$ is the solution of the following PDE (Partial Derivative Equation):

$$L\, \delta = F(\phi(t)), \tag{13}$$

with $\phi(t) = \mathrm{Id} + u(t)$ and F defined as in equation (11).

3.2. Algorithm Discretization

For the implementation of algorithm 1, equation (13) is discretized following the Galerkin method [13]. First, it can be noticed that equation (13) is formally equivalent to the variational equation:

$$\forall\ v \in \mathcal{W}_3,\ \ A_{\Omega_1}(\delta, v) = \langle F(\phi(t)), v \rangle_{\Omega_1}, \tag{14}$$

where F is defined in equation (11). We choose a space $\mathcal{W}^h$ of dimension h which is included in $\mathcal{W}_3$ and spanned by a finite family of functions with compact support. We will denote by ψ^h_i the functions of this family, where i is an index varying in a finite set I_h of size h. In order

to approximate the solution of equation (14), we find in $\mathcal{W}^h$ the solution of the approximate variational equation:

$$\forall\, v \in \mathcal{W}^h,\ \ A_{\Omega_1}(\delta, v) = \langle F(\phi(t)), v\rangle_{\Omega_1}. \tag{15}$$

The solution of this equation is

$$\delta^h = \sum_{j\in I_h} \beta_j^h\, \psi_j^h, \tag{16}$$

where the coefficients β_j^h are the solution of the linear system:

$$\forall\, i \in\ I_h,\ \ \sum_{j\in I_h} \beta_j\, A_{\Omega_1}(\psi_j^h, \psi_i^h) = \langle F(\phi(t)), \psi_i^h\rangle_{\Omega_1}. \tag{17}$$

In order to design the approximation spaces $\mathcal{W}^h$, the set Ω_1 is decomposed into $h/2$ fixed-size non-overlapping squares. We define $\mathcal{W}^h$ as the space formed by the functions that are C^1 on Ω_1 and polynomial on each of these squares. The design of the function family $\{\psi_i^h\}_{i\in I_h}$ is based on spline functions.

When decomposed, the domain Ω_1 may be slightly approximated near the boundaries. This may cause segmentation inaccuracies. However, these inaccuracies are taken into account in model 3 via the estimation of S (see section 2.3).

3.3. Initialization Step

Unlike model 2, the contour match is not used for the design of model 3. However, it is worth using it to have a better initialization of the dynamic system. Hence we define the displacements M_0 in equation (12) as the solution of the problem in model 2 when γ_1 is equal to zero. The displacements M_0 are the same as those which are obtained at the initialization step of the algorithm of model 2 [45, 47]. Let us denote by $\mathcal{W}_0$ the space composed of the functions of $\mathcal{W}_2$ (see section 2.2) and equal to the identity map Id on $\partial\Omega_1$. The displacements M_0 are equal to $u_0 + \delta_0$, where u_0 is defined in section 2.2 and δ_0 is the solution in $\mathcal{W}_0$ of the following variational equation:

$$\forall\, v \in \mathcal{W}_0,\ A_{\Omega_1}(\delta, v) = -A_{\Omega_1}(u_0, v). \tag{18}$$

Using the Galerkin method (see section 3.2), δ_0 can be approximated by the displacements δ_0^h which are found as follows:

$$\delta_0^h = \sum_{j\in I_h} \beta_{j,0}^h\, \psi_j^h\ \in \mathcal{W}_0^h, \tag{19}$$

where the coefficients $\beta_{j,0}^h$ are the solution of the linear system

$$\forall\, i \in I_h,\ \ \sum_{j\in I_h} \beta_{j,0}^h\, A_{\Omega_1}(\psi_j^h, \psi_i^h) = -A_{\Omega_1}(u_0, \psi_i^h). \tag{20}$$

3.4. Multigrid Implementation

In order to lower computation times and obtain better minimization results, we adopt a multigrid implementation approach together with a coarse-to-fine strategy. We define a series

$\{\mathcal{W}^{h(k)}\}_{k\in\mathbb{N}}$ of embedded subspaces having the properties described in section 3.2:

$$\mathcal{W}^{h(1)} \subset \cdots \subset \mathcal{W}^{h(k)} \subset \cdots \subset \mathcal{W}_3.$$

The dynamic system is discretized with respect to time using the Euler method. We obtain the following resolution scheme:

Algorithm 2 (multigrid implementation)

Initialization: $u(0) = u_0 + \delta_0^{h(K)}$,

where u_0 is defined in section 2.2 and $\delta_0^{h(K)}$ is the solution in a space $\mathcal{W}_0^{h(K)}$ of equations (19) and (20).

$\mathbf{k^{th}}$ ***Iteration*** *($k \geq 0$) :* $u(k+1) = u(k) + \epsilon\ \delta(k)$,

where ϵ is a small positive value and $\delta(k)$ is the solution in $\mathcal{W}^{h(k)}$ of equations (16) and (17) with t equal to k.

4. Application to mammogram pairs

In this section, we apply the different models described in section 2 to mammogram pairs. In section 4.1, the application context and goal are presented. In section 4.2, some preliminary remarks are given about preprocessing, parameter choices and mammograms used. Section 4.3 gives some evaluations and comparisons of the algorithm performances based on simulated mammogram pairs. In section 4.4, we illustrate the algorithm applications to real mammogram pairs.

4.1. Application Context and Goal

Radiologists use several methods to analyze mammograms for the detection of abnormalities [56]. One of these methods consists of seeking deviations from normal breast symmetry by comparison of left and right breast mammograms (same view angles) . This method is helpful to locate abnormalities which are difficult to detect based on single image analysis. As an illustration, comparing bilateral mammograms of figures 4.1 (a) and 4.1 (b), a significant bright region asymmetry can be observed in the circled area. Focusing on this asymmetry area in the right mammogram, a small bright region which indicates a tumor (a spiculated mass) can be detected. This tumor contrasts poorly with the surrounding tissues and would have been difficult to locate using only the right mammogram. A detection approach which is similar to the asymmetry approach consists in looking for abnormal temporal changes in different mammograms of the same breasts (same view angles) .

The comparison of bilateral or temporal mammogram pairs is also an approach for the design of CAD (Computer Aided Diagnosis) systems devoted to the automatic tumor detection (see [2, 21, 62] for CAD in mammography). The techniques which follow this approach can be classified into two categories. The first type of techniques compares regions of mammograms [9, 31, 33, 34, 42, 59, 60, 61, 63]. The main difficulty encountered in the design of such a technique is the segmentation and matching of mammogram regions of interest. The second kind of techniques compare locally mammograms without using regions of interest [23, 29, 36, 40, 39, 45, 47, 48, 49, 51, 53, 54, 66, 67, 68]. The main problem of this approach is to compensate for normal mammogram differences which are locally similar to abnormalities and generate high false-positive rates. These normal differences can be due to acquisition process condition changes, breast positioning and breast compression level variations and anatomical

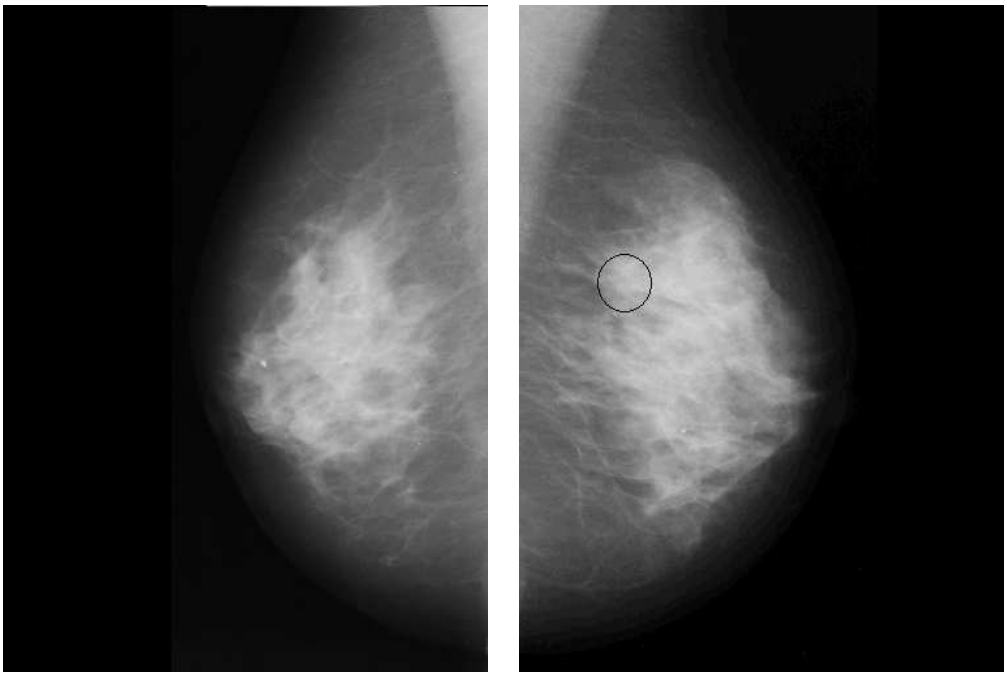

(a) (b)

Figure 4. A pair of bilateral mammograms showing an abnormal asymmetry.

or histological variations. Differences resulting from acquisition condition changes are often very sharp in temporal mammogram pairs. They can be compensated for by a mammogram normalization [24, 25, 28, 33, 35]. Differences due to breast positioning can be easily compensated for by an alignment procedure which involves rotation and translation and are based on breast contours [23, 36, 53, 54, 66, 67]. The effects of the other factors (breast compression level, histology and anatomy variations) on mammogram appearance are not well-known; in particular, modeling compression effects is an important and quite recent topic of research [4, 5, 6, 25, 26, 27, 32, 43]. For differences due to the three last factors to be compensated for, it is necessary to register pairs of mammograms. Main works on mammogram registration can be found in [29, 36, 40, 39, 41, 45, 47, 48, 50, 52]. These works were discussed in introduction.

In mammograms, textures and finest details might be very dissimilar from one image to the other. Hence mammograms cannot be registered at finest scales. This paper concerns only the registration of normal structures which are present in mammograms at a coarse scale (essentially, muscles and salient bright regions of breasts). The registration aim is to compensate accurately for differences between the coarse structures and, consequently, to enhance differences due to small tumors. Our final goal is to detect tumors in mammograms by analyzing the registered mammogram differences and the deformation fields. The tumor detection is beyond the scope of this paper. The interested readers may find more details and some trials based on model 2 in [45].

4.2. Some preliminary remarks

The next experiments are based on bilateral mammogram pairs which are shown in figures 12 (a) and 12 (b), figures 13 (a) and 13 (b) and figures 14 (a) and 14 (b). These images comes from the MIAS database [55] and have a resolution of 200 microns. These image pairs were chosen in the different classes of the database. As a consequence, the breast aspect is very different from one pair to the other. In the first pair, the aspect is of "dense" type (bright aspect), in the second one, it is of "fatty" type (dark aspect) and in the third one, it is of "glandular" type (between fatty and dense aspects).

In each mammogram, the breast region was automatically segmented. The segmentation technique is based on a threshold which is the value of the gray-level corresponding to the first peak in the smoothed histogram of the image. After thresholding, the biggest connected region (the breast) is located. The breast contour is smoothed using an approximation technique based on B-splines [19].

The registration models are applied to images which are coarse approximations of the original mammograms (see section 4.1). In order to obtain these images, mammograms are smoothed using an approximation technique based on B-splines [19, 45].

In the next experiments, the value of the weight γ_1 of the intensity-based registration term in models 2 and 3 is fixed at 1. The Lame coefficients λ and μ of the regularity term (equation 2) are fixed at 10^{-12} and 500 respectively. These values are fixed using the Poisson ratio ν and the Young modulus E. The Lame coefficients μ and λ are related to ν and E by equations $\mu = \frac{E}{2(1+\nu)}$ and $\lambda = \frac{E\nu}{(1+\nu)(1-2\nu)}$ [14]. The Poisson ratio takes values in $]0, 0.5[$. When far enough from 0.5, variations of the Poisson ratio values does not affect mammogram registrations obtained using model 2 [45]. The Poisson ratio value is fixed arbitrarily at 10^{-15}. In models of section 2, the Young modulus can be interpreted as a weight of the regularity term. We fixed its value as follows. We apply model 2 to the first mammogram pair with different values of the Young modulus. We choose the lowest value which enables to register significantly the first mammogram pair without obtaining a singular solution ($E = 10^3$). Despite the mammogram aspect differences outlined above, the selected values for μ, λ and γ_1 turned out to be suitable for the application of models 2 and 3 to the three image pairs (see section 4.4). This suggests that parameters could be chosen optimally for the application of models to mammogram pairs of a same database.

The algorithms of models 2 and 3 were implemented on a PC Intel Penthium II 600 MHz. The computation time of both algorithms is approximately the same. It is between 5 and 8 minutes when applied to mammograms having approximately 450000 pixels on average.

4.3. Application to simulated mammogram pairs

Couples of images in figures 5 (a) and 5 (d), figures 6 (a) and 6 (b) and figures 7 (a) and 7 (b) are three simulated mammogram pairs. In these simulated pairs $(I^0, I^1_\star)$, $I^1_\star$ is a geometric deformation of I^0 ($I^1_\star = I^0 \circ \phi^\star$) obtained with a known function $\phi^\star$. The functions $\phi^\star$ were obtained after application of model 2 to the original mammogram pairs shown in figures 12 (a) and (b), figures 13 (a) and (b), figures 14 (a) and (b), respectively.

Model 2 was applied to each simulated image pair $(I^0, I^1_\star)$ with the exact initialization derived from $\phi^\star$. In each case, a solution denoted by ϕ_{ref} was obtained. As can be seen in figures 5 (b), 6 (c) and 7 (c), the image pairs were almost perfectly registered by model 2. The image differences were respectively lowered by 80.8, 80.5 and 79.9 percent and the mean distances between the

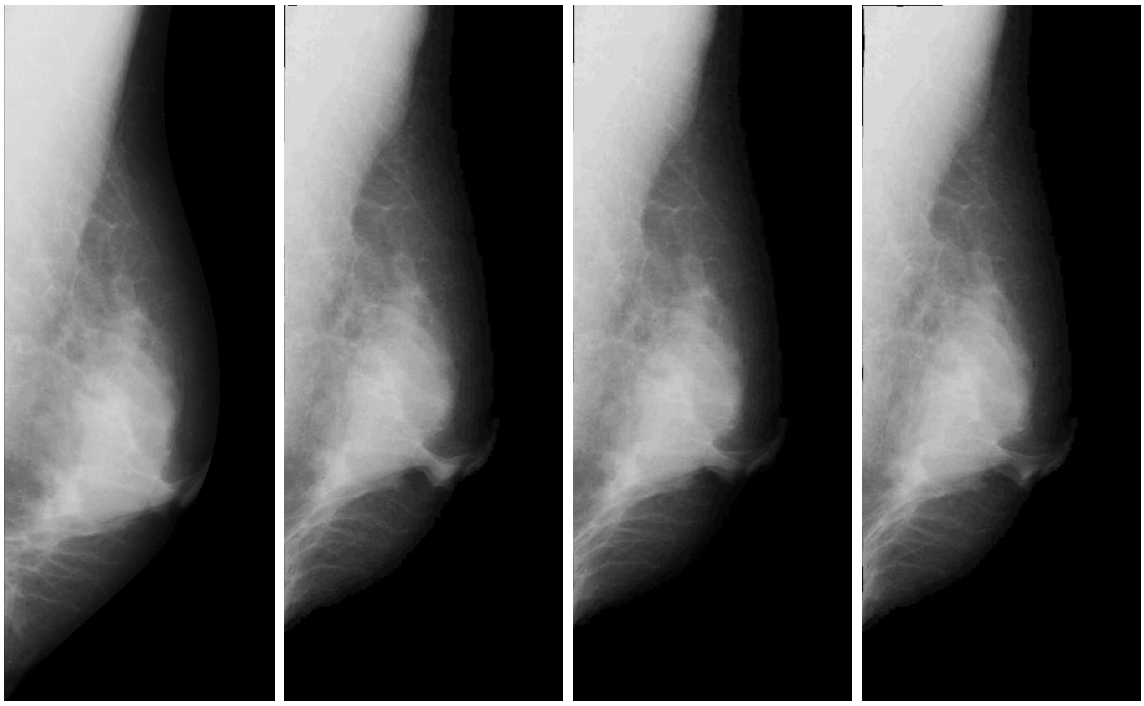

(a) (b) (c) (d)

Figure 5. Application to a first simulated mammogram pair: (a) The source image I^0, the geometric deformation I^0_ϕ of I^0 after the application of (b) model 2 and (c) model 3, (d) the target image $I^1_\star$. The target image $I^1_\star$ was obtained by applying a deformation $\phi^\star$ to the source image I^0 ($I^1_\star = I^0 \circ \phi^\star$).

algorithm solution ϕ_{ref} and the exact mapping $\phi^\star$ were respectively 3.8, 5.4 and 4.3 pixels. The image registration benefits from the region-specific constraints: Model 1 lowered the image differences by only 68, 70 and 64.3 percent, respectively (for a more extensive comparison of models 1 and 2, the interested reader may refer to [45]). In this context, model 2 is the most relevant among the three models described in section 2 since the boundary conditions are exact. Using model 3 with $\gamma_2 = 1000$, the image differences were respectively lowered by 78, 77.2 and 77 percent.

For each simulated mammogram pair, we simulate five wrong initialization functions ϕ_0 defined on the breast contour of $I^1_\star$ (see sections 2.2 and 3.3). Typical wrong initializations are shown in figures 8 (a) and 8 (b). Comparing the yellow and pink lines, it can be seen that, these initialization functions do not correctly map into the breast contour in I^0. Models 2 and 3 were applied to the pairs $(I^0, I^1_\star)$ with the wrong initialization functions. The mean results for the three pairs are shown in table 1. In all cases, it can be observed that the registration performance of model 2 is drastically reduced due to the initialization errors. With wrong initializations, the image differences are respectively lowered by only 69.9, 66.1 and 64.7 percent on average. Moreover, the solution regularity is decreased. The regularity term reaches the mean values 344.5, 506.5 and 309 with wrong initializations whereas they were only 117, 450 and 260

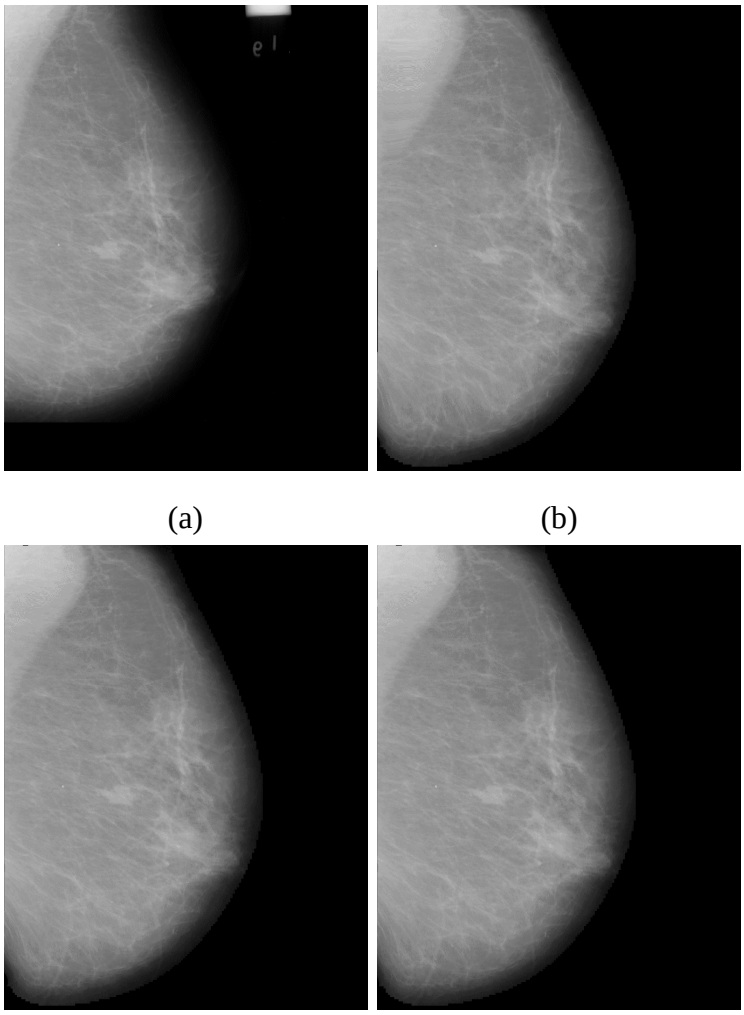

(a) (b)

(c) (d)

Figure 6. Application to a second simulated mammogram pair: (a) The source image I^0, (b) the target image $I^1_\star$. The geometric deformation I^0_ϕ of I^0 after the application of (c) model 2 and (d) model 3. Images (a) and (b) form a simulated pair of mammograms. The target image $I^1_\star$ was obtained by applying a deformation $\phi^\star$ to the source image I^0 ($I^1_\star = I^0 \circ \phi^\star$).

with the exact initializations. These regularity decreases are due to some compressions or dilatations which occur near contours. Such compressions and dilatations are shown in figures 9 (a) and 10 (a). They are caused by the opposition of the two registration constraints (the one of the fixed and wrong boundary conditions and the one of the intensity-based energy term).

Model 3 is more robust than model 2 to the initialization errors. Indeed, the registration scores of model 3 are higher than those of model 2 (over 73 percent on average in all cases) and its solutions are smoother. Comparing figures 9 (a) and 9 (b) and figures 10 (a) and 10 (b), it can also be observed that the compressions and dilatations near the contours are less pronounced in the solutions of model 3 than in those of model 2. The robustness of model 3 is further

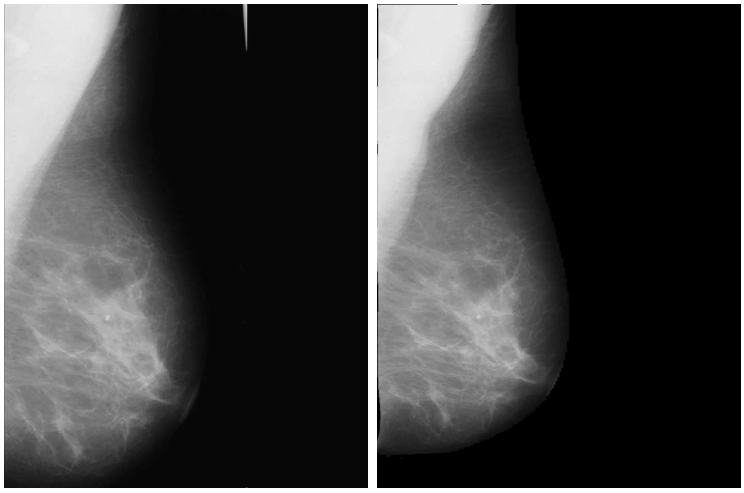

(a) (b)

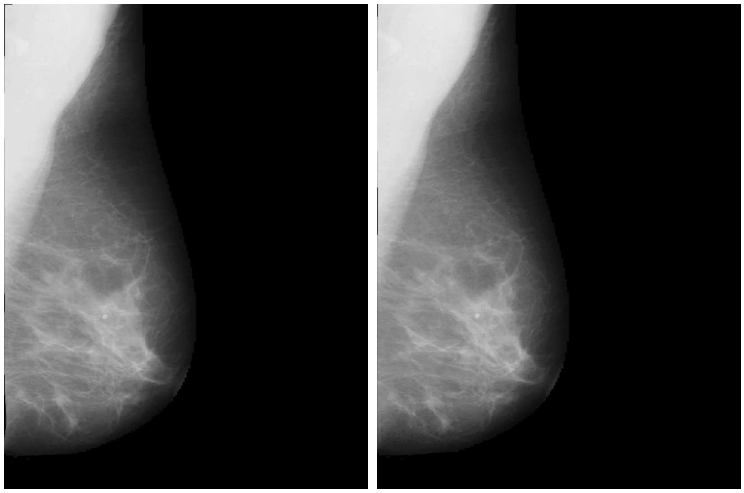

(c) (d)

Figure 7. Application to a third simulated mammogram pair: (a) The source image I^0, (b) the target image $I^1_\star$. The geometric deformation I^0_ϕ of I^0 after the application of (c) model 2 and (d) model 3, (d) the target image $I^1_\star$. Images (a) and (b) form a simulated pair of mammograms. The target image $I^1_\star$ was obtained by applying a deformation $\phi^\star$ to the source image I^0 ($I^1_\star = I^0 \circ \phi^\star$).

attested by the comparisons of the algorithm solutions and the reference solution ϕ_{ref} (solution of model 2 without initialization errors). Means and standard deviations of distances between the solutions obtained with different models and ϕ_{ref} are shown in table 2 for each simulated cases. It can be seen that model 2 is more sensitive to initialization errors than model 3. In all simulated cases, means and standard deviations obtained for model 2 are higher than those obtained for model 3 . Standard deviations for model 3 are low. Model 3 is stable when the initialization varies.

Besides, in table 1, it can be noticed that performances of model 3 improves as the weight

(a) (b)

Figure 8. Correction effect due to the segmentation term of model 3. Figures (a) and (b) show two different examples of segmentation results obtained after image registration with wrong initialization. In figures (a) and (b), the yellow line is the correct segmentation of the breast and the pink one is the segmentation which is induced by the wrong initialization map ϕ_0. The blue and red lines are the segmentations that are induced by the solutions of model 3 with γ_2 equal to 0 and 1000 respectively.

γ_2 of the segmentation term increases. When model 3 is used with γ_2 equal to 1000, not only registration scores are good and close to those of solutions ϕ_{ref} but also standard deviations are low. This shows that the segmentation term in model 3 is a factor of robustness.

Moreover, mammograms are much better registered near the contours when γ_2 is high. As an illustration, we can compare image differences in figures 11 (a) and 11 (b). Figures 8 (a) and 8 (b) show the segmentations of I^0 which are induced by the algorithm solutions. It can be seen

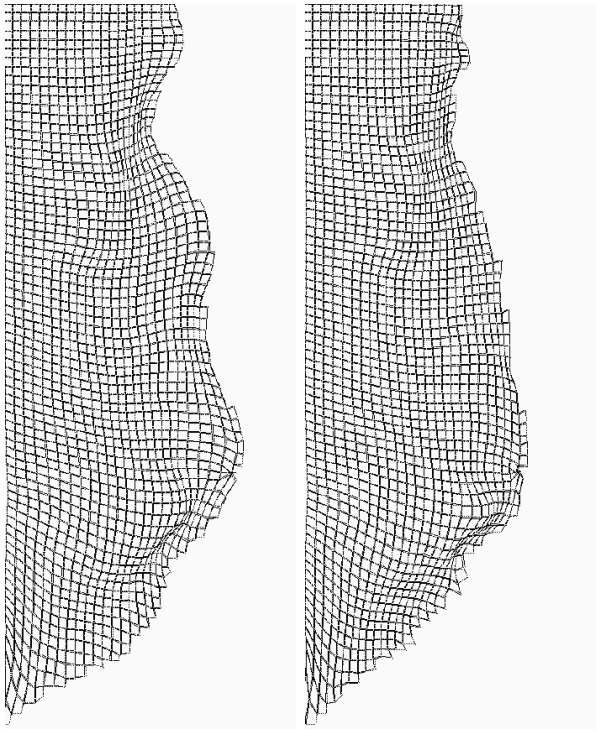

(a) (b)

Figure 9. First simulation case. Images (a) and (b) show an example of images $\phi(\Omega_1)$ of the tessellated breast domain Ω_1 in $I_\star^1$ by the solutions ϕ which are obtained using model 2 (image (a)) and model 3 ($\gamma_2 = 1000$) (image (b)) with a same wrong initialization. In image (a), a strong compression due to initialization errors can be observed near the nipple position.

that the segmentation obtained with model 3 when γ_2 is high is close to the right segmentation whereas the segmentation obtained with model 3 when γ_2 is low remains close to the wrong initialization segmentation. In model 3, the segmentation term is necessary for the initialization errors to be compensated for.

In this section, the experiments were done using three mammograms with different breast aspects (see section 4.2). Despite these differences, the behavior and the performances of model 3 are equivalent on the three simulated pairs for each value of the parameter γ_2. Results in tables 1 and 2 suggest that the value of γ_2 could be set to 1000 for the application of model 3 to mammogram pairs of the MIAS database. When the parameter γ_2 is equal to 1000, the algorithm obtains the best mean registration score and is stable when the initialization varies (the standard deviations mentioned in tables are low).

In the previous experiments, simulations were only with respect to geometric deformations. More general simulations would include anatomic variations. Such experiments are beyond the scope of this paper. The interested reader can find several simulated experiments about anatomic variations due to tumors in [45].

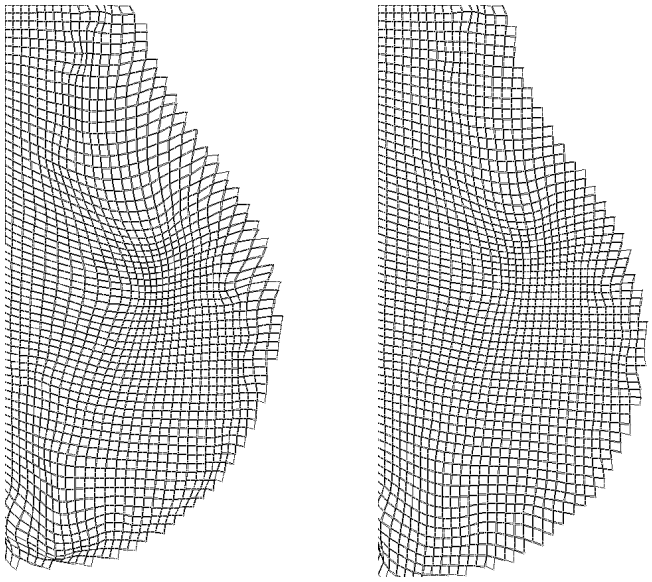

(a) (b)

Figure 10. Third simulation case. Images (a) and (b) show an example of images $\phi(\Omega_1)$ of the tessellated breast domain Ω_1 in $I_\star^1$ by the solutions ϕ which are obtained using model 2 (image (a)) and model 3 ($\gamma_2 = 1000$) (image (b)) with a same wrong initialization. In image (a), a strong dilatation due to initialization errors can be observed near the contour in the top of image.

4.4. Application to real mammogram pairs

Comparing bilateral mammogram in figures 12 (a) and 12 (b), figures 13 (a) and 13 (b) and figures 14 (a) and 14 (b) and observing image differences in figures 15 (a), 16 (a) and 17 (a), it can be noticed that mammograms have a lot of important asymmetries, due in particular to breast shape variations. Next, looking at source images I^0 in figures 12 (a), 13 (a) and 14 (a) and at their geometric deformations I_ϕ^0 in figures 12 (c),13 (c) and 14 (c), it can be seen that the initialization step changes breast shapes in I^0. As observed in figures 15 (b), 16 (b) and 17 (b), these changes significantly compensate not only for the asymmetries near the breast contours but also for some inner differences. However, due to preprocessing step inaccuracies and to the algorithm discretization (see section 3.2), the breast contour asymmetries are not perfectly compensated for. For instance, in figure 16 (b), it can be observed a dark border in the upper part of the contour area. Moreover, several important inner differences remain in the registered image pair.

Some of these inner differences are due to shape and location variations of bright salient regions of images. Comparing pairs of deformed images in figures 12 (b) and 12 (d), figures 13 (b) and 13 (d), figures 14 (b) and 14 (d) and looking at images of figures 15 (c), 16 (c) and 17 (c), it can be seen that these particular differences are compensated for using model 2. However, several differences still remain in the pair of images registered by model 2. Some of these differences are caused by breast tissue disparities and cannot be corrected by any geometric deformation.

Model			Case 1		Case 2		Case 3	
			Means	Std Dev.	Means	Std Dev.	Means	Std Dev.
Initialization		Rs.	19.7 %	18.4	28.2 %	25.3	25.8 %	7.8
Step		Rl.	295.5	124.1	424	512.8	256	145
2		Rs.	69.9 %	2.4	66.1 %	6.8	64.7 %	14.4
		Rl.	344.2	139.2	506.5	460.2	309	141
3	γ_2	Rs.	74.1 %	3.9	73.6 %	6.9	75.1 %	1.6
	$= 0$	Rl.	301	129.8	481	335.8	452	151
	γ_2	Rs.	75.5 %	3.2	75 %	5.1	75.8 %	1.2
	$= 500$	Rl.	298.6	130.0	493	329.5	449	148.7
	γ_2	Rs.	76.9 %	1.8	75 %	4.9	76.6 %	1.3
	$= 10^3$	Rl.	300	129.1	495.2	327.3	448	149
	γ_2	Rs.	76.1%	1.1	75.1 %	4.1	78.4 %	2.2
	$= 10^4$	Rl.	313.8	128.2	563	297.7	436	136

Table 1
Comparison of the applications of models 2 and 3 with wrong initializations. The rows “Rs.” give the image registration scores (in percentage of the initial quadratic difference between I^0 and I^1): $100 \cdot (|I^0 - I^1|^2 - |I^0_\phi - I^1|^2)/|I^0 - I^1|^2$. The rows “Rl.” give the values of the regularity term (equation (2)). The column “Means” gives the means of the registration and regularity scores of the algorithms with five different wrong initializations and the column “Std Dev” the standard deviations of these scores.

However, these registrations can be improved. In particular, in the registered image differences (figures 15 (c), 16 (c) and 17 (c)), we still observe the contour differences which remained after the initialization. These differences cannot be compensated for using model 2 due to the fixed boundary conditions. Besides, some important differences remain near contours; for instance, see differences near the nipple position in figure x15 (c) or in the upper part of image in figure 16 (c). Model 2 is unable to correct such differences for the following reason. The differences increase the intensity-based registration constraint in a way that conflicts with the contour-based constraint. As can be noticed in figures 18 (b), 19 (b) and 20 (b), constraint conflicts generate strong compressions or dilatations in difference areas. Further difference corrections are not possible because they would increase compressions (or dilatations) and regularity term values (equation (2)).

These results are in sharp contrast with those of model 3. We recall that, in this model, the boundary conditions are free. Consequently, the contour constraint of model 2 is less stringent. This constraint relaxation permits a better registration of the images near the breast contours. Looking at deformed images in figures 12 (e), 12 (b), 13 (e), 13 (f), 14 (e) and 14 (f) and at

	model 2	model 3 ($\gamma_2 = 0$)	model 3 ($\gamma_2 = 1000$)
First simulation case			
Mean distances	9.6	7.1	6.1
Distance standard deviations	7.1	3.2	3.1
Second simulation case			
Mean distances	9	7.7	7.6
Distance standard deviations	4.6	3.3	3.2
Third simulation case			
Mean distances	12.6	9.6	8.8
Distance standard deviations	8.6	1.8	1.2

Table 2
Means and standard deviations of distances between ϕ_{ref} (solution of model 2 with the exact initialization) and solutions obtained using different models with initialization errors.

registered image differences in figures 15 (d), 15 (e), 16 (d), 16 (e), 17 (d), 17 (e), it can be observed that model 3 (with different values of weight γ_2) succeeds in compensating significantly for the differences near contours. Moreover, as can be observed in figures 18 (c), 18 (d),19 (c), 19 (d), 20 (c) and 20 (d), the deformations are less compressed and dilated near contours and smoother than the ones obtained with model 2. As can be observed in figures 15 (d), 15 (e), 16 (d), 16 (e), 17 (d) and 15 (e), model 3 without the segmentation term ($\gamma_2 = 0$) may map some parts of the breast in I^1 into some parts of the background in I^0 whereas model 3 with a strong segmentation constraint keeps mappings inside breast regions of I^0.

5. Conclusion

Based on a variational approach, we formulated a new mathematical model for mammogram registration. An energy minimization problem was presented. A multigrid gradient descent algorithm was designed for the numerical resolution of the problem. As in [45, 47], the model focuses on the matching of regions of interest. It also combines segmentation-based and intensity-based constraints. However, the energy minimization problem is not posed with fixed boundary conditions but with free boundary conditions. Moreover, the energy has a new registration constraint. The performances of both models were compared on simulated mammogram pairs. It was shown that the new model is more robust to the initialization inaccuracies than the previous one. The ability of the new model to compensate for these inaccuracies during the matching process was also illustrated. Both models were applied to real mammogram pairs in order to illustrate the interest of the new model in the application context. Although it was designed for the mammogram registration, the model is generic: it can be applied whenever the

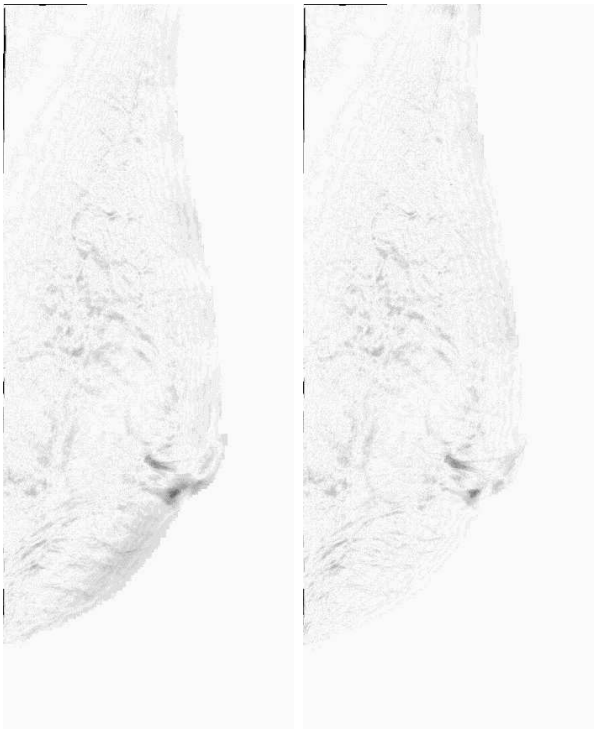

(a) (b)

Figure 11. First simulation case. Figures (a) and (b) show the absolute differences between images $I^1_\star$ and $I^0 \circ \phi$ (first simulation case) where ϕ are the solutions found using model 3 with $\gamma_2 = 0$ (figure (a)) and with $\gamma_2 = 1000$ (figure (b)). **[black=high differences, white=low differences]**

images have single regions of interest. We believe that, in these common cases, the new model is better suited for image registration than the usual intensity-based models. In particular, it could be powerful for the mapping of brain anatomical templates onto individual anatomies.

REFERENCES

1. Y. Amit. A non-linear variational problem for image matching. *SIAM Journal on Scientific Computing*, 15(1):207–224, January 1994.
2. S. Astley, I. Hutt, S. Adamson, et al. Automation in mammography: computer vision and human perception. In K. W. Bowyer and S. Astley, editors, *State of the Art in Digital Mammographic Image Analysis*, Series in Machine Perception and Artificial Intelligence vol. 9, pages 1–25. World Scientific, 1994.
3. R. Bajcsy and S. Kovacic. Multiresolution elastic matching. *CVGIP*, 46:1–21, 1989.
4. P. Bakic, M. Albert, and D. Brzakovic. Evaluation of a mammography simulation. In M. Yaffe, editor, *Proc. of the 5th International Workshop on Digital Mammography*, pages 681–687, Toronto, Canada, June 2000. Medical Physics Publishing.
5. P. Bakic, D. Brzakovic, P. Brzakovic, et al. An approach to using a generalized breast model

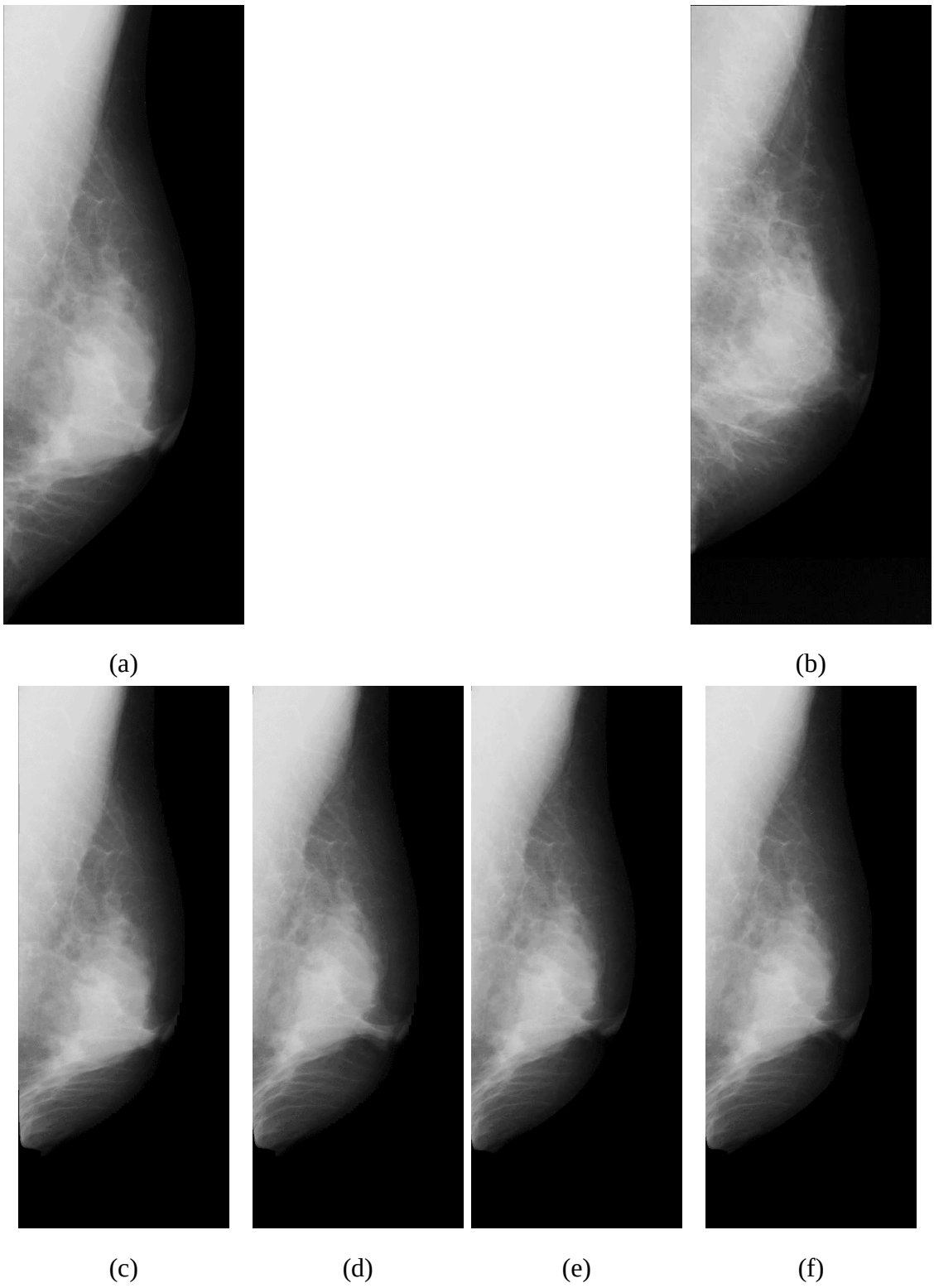

Figure 12. Bilateral mammograms # 035/036 (MIAS database). (a) The source image I^0, (b) the target image I^1. The geometric deformation I^0_ϕ of I^0 (c) after the initialization step, after the application of (d) model 2, (e) model 3 with γ_2 equal to 0, (f) model 3 with γ_2 equal to 1000.

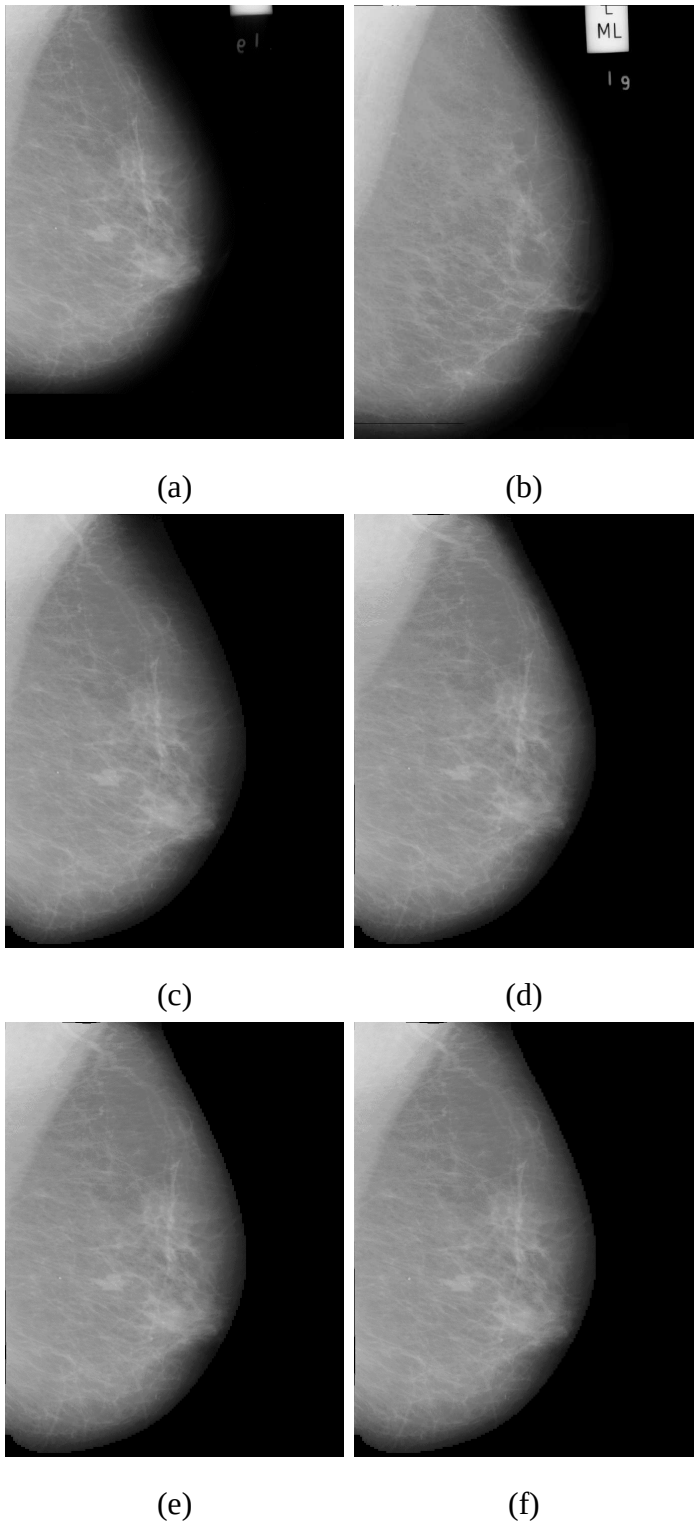

(a) (b)

(c) (d)

(e) (f)

Figure 13. Bilateral mammograms # 077/078 (MIAS database). (a) The source image I^0, (b) the target image I^1. The geometric deformation I^0_ϕ of I^0 (c) after the initialization step, after the application of (d) model 2, (e) model 3 with γ_2 equal to 0, (f) model 3 with γ_2 equal to 1000.

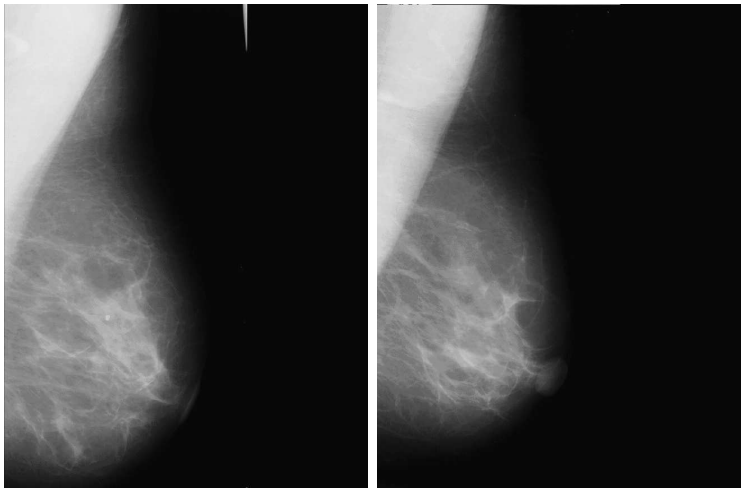

(a) (b)

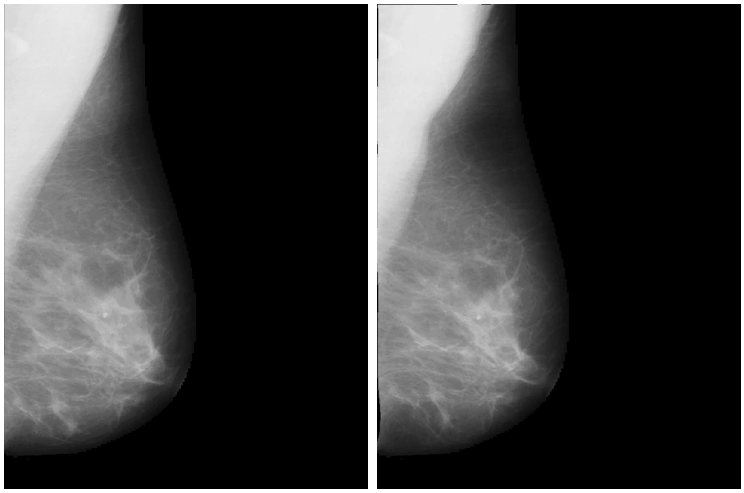

(c) (d)

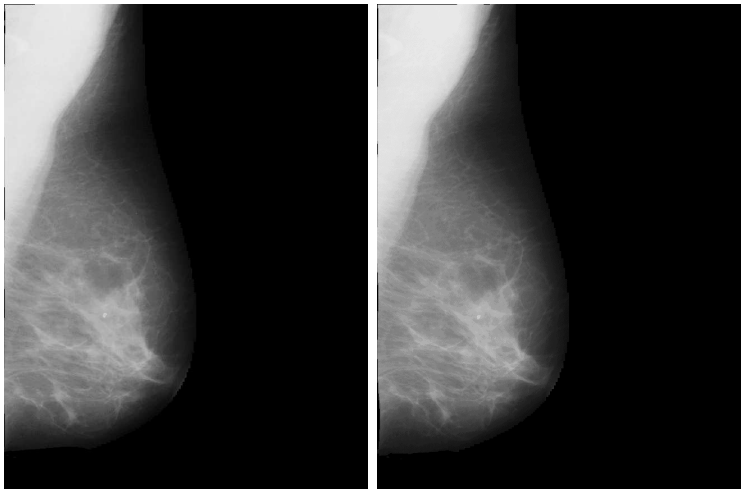

(e) (f)

Figure 14. Bilateral mammograms # 047/048 (MIAS database). (a) The source image I^0, (b) the target image I^1. The geometric deformation I^0_ϕ of I^0 (c) after the initialization step, after the application of (d) model 2, (e) model 3 with γ_2 equal to 0, (f) model 3 with γ_2 equal to 1000.

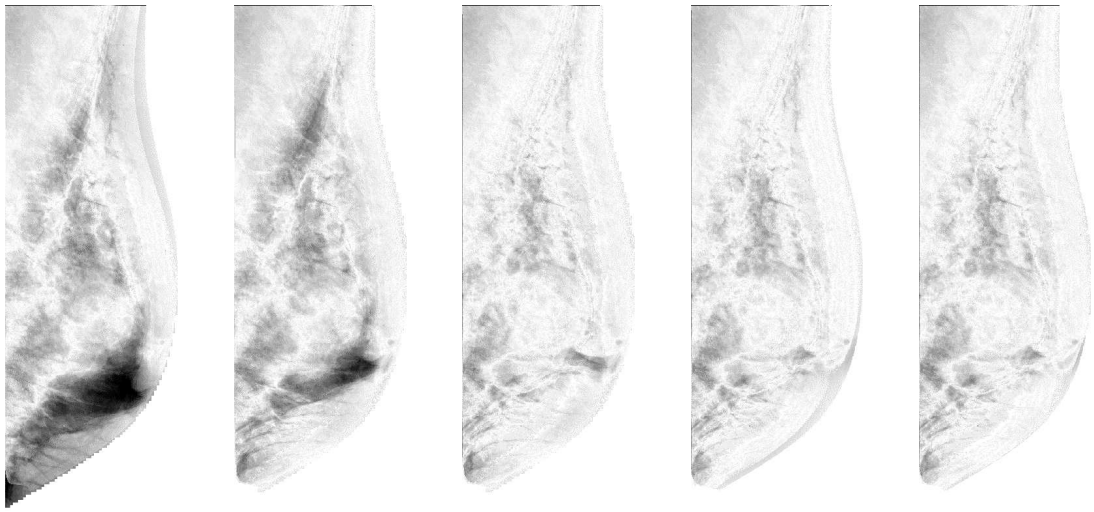

(a) (b) (c) (d) (e)

Figure 15. Bilateral mammograms # 035/036. The absolute differences between image I^1 and (a) I^0, (b) the deformed image I^0_ϕ after the initialization step, (c) the deformed image I^0_ϕ after the application of model 2, (d) the deformed image I^0_ϕ after the application of model 3 with γ_2 equal to 0, (e) the deformed image I^0_ϕ after the application of model 3 with γ_2 equal to 1000 **[black=high differences, white=low differences]**.

to segment digital mammograms. In *Proc. of 11th IEEE Symposium on Computer-Based Medical Systems*, pages 84–89, Lubbock, 1998.

6. C. Behrenbruch, M. Yam, M. Brady, et al. The use of magnetic resonance imaging to model breast compression in x-ray mammography for mr/x-ray data fusion. In M. Yaffe, editor, *Proc. of the 5th International Workshop on Digital Mammography*, pages 688–696, Toronto, Canada, June 2000. Medical Physics Publishing.
7. F.L. Bookstein. Principal warps: thin-plate splines and the decomposition of deformations. *IEEE PAMI*, 11(6):567–585, 1989.
8. C. Broit. *Optimal Registration of deformed images*. PhD thesis, University of Pennsylvania, 1981.
9. D. Brzaković, N. Vujović, M. Nesković, et al. Mammogram analysis by comparison with previous screenings. In A.G. Gale et al., editors, *Proc. of the 2nd International Workshop on Digital Mammography*, pages 131–139, York, England, July 1994. Elsevier Science.
10. D.J. Burr. A dynamic model for image registration. *CVGIP*, 15:102–112, 1981.
11. G.E. Christensen, R.D. Rabbitt, and M.I. Miller. Deformable templates using large deformation kinematics. *IEEE IP*, 5(10):1435–1447, October 1996.
12. G.E. Christensen, R.D. Rabbitt, and M.I. Miller. Mathematical textbook of deformable neuroanatomies. In *Proc. Natl. Acad. Sci., USA*, volume 90, pages 11944–11948, dec 93.
13. P. G. Ciarlet. *The finite element method for elliptic problems*. North-Holland, Amsterdam, 1978.

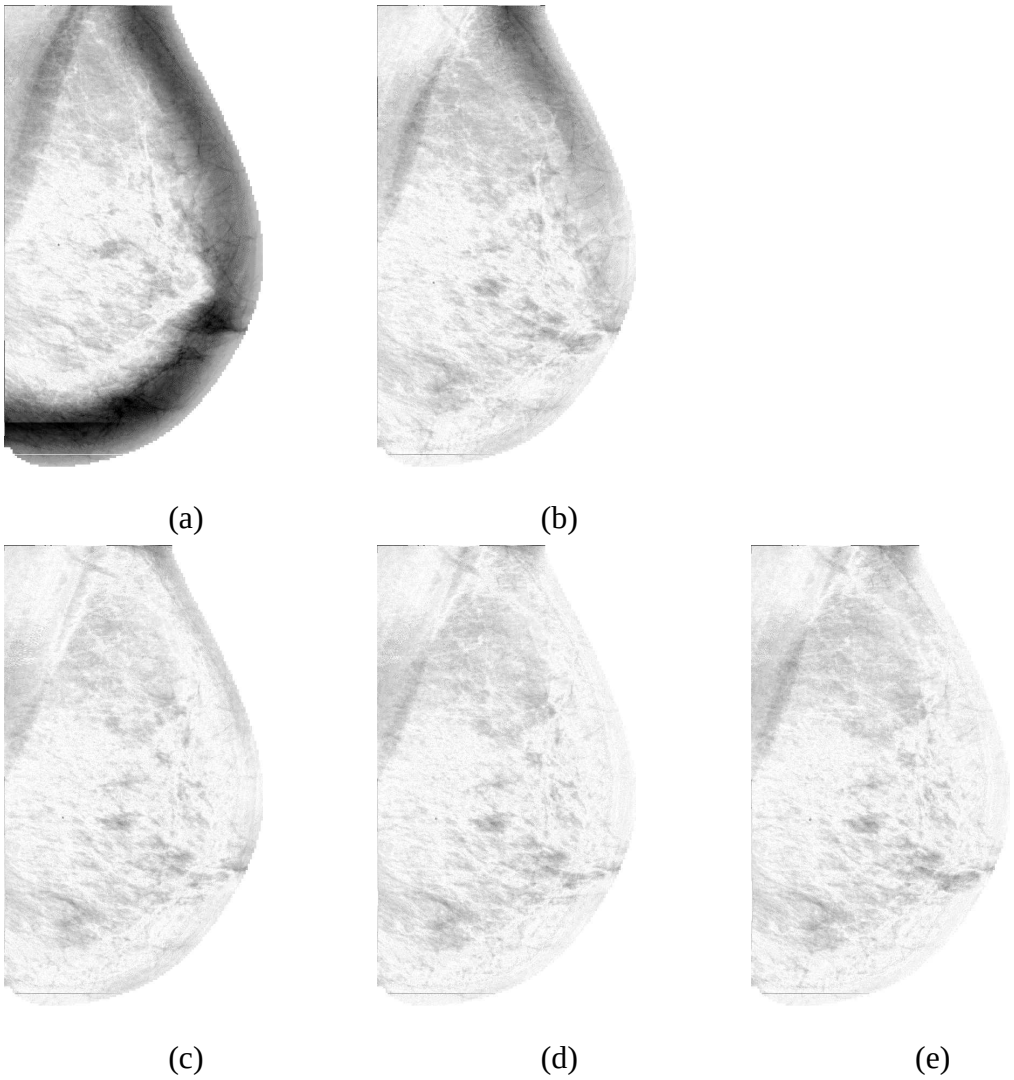

Figure 16. Bilateral mammograms # 077/078.The absolute differences between image I^1 and (a) I^0, (b) the deformed image I^0_ϕ after the initialization step, (c) the deformed image I^0_ϕ after the application of model 2, (d) the deformed image I^0_ϕ after the application of model 3 with γ_2 equal to 0, (e) the deformed image I^0_ϕ after the application of model 3 with γ_2 equal to 1000 **[black=high differences, white=low differences]**.

14. P.G. Ciarlet. *Mathematical elasticity, volume 1: three-dimensional elasticity*. Studies in Mathematics and its Applications. North-Holland, Amsterdam, 1988.
15. L. D. Cohen. On active contour models and balloon. *Computer Vision, Graphics, and Image Processing : Image Understanding*, 53(2):211–218, 1991.
16. L. D. Cohen and I. Cohen. Finite-element methods for Active Contour models and Balloons for 2D and 3D images. *IEEE PAMI*, 15(11):1131–1147, 1993.
17. Laurent D. Cohen. Avoiding local minima for deformable curves in image analysis. In C. Rabut A. Le Méhauté and L. L. Schumaker, editors, *Curves and Surfaces with Applica-*

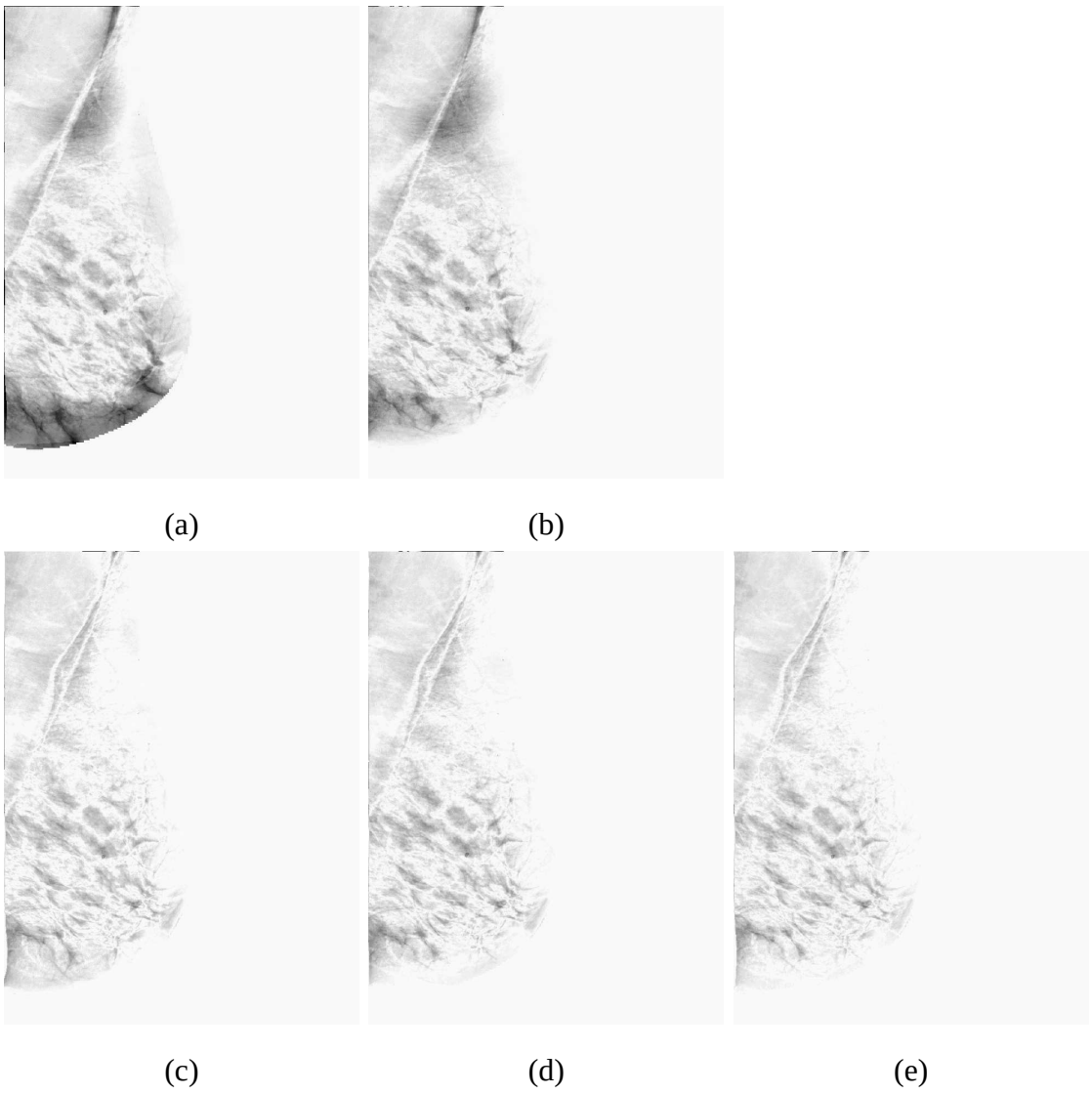

(a) (b)

(c) (d) (e)

Figure 17. Bilateral mammograms # 047/048.The absolute differences between image I^1 and (a) I^0, (b) the deformed image I^0_ϕ after the initialization step, (c) the deformed image I^0_ϕ after the application of model 2, (d) the deformed image I^0_ϕ after the application of model 3 with γ_2 equal to 0, (e) the deformed image I^0_ϕ after the application of model 3 with γ_2 equal to 1000 **[black=high differences, white=low differences]**.

tions in CAGD, pages 77–84, 1997.

18. C. Davatzikos. Spatial transformation and registration of brain images using elastically deformable models. *Computer Vision and Image Understanding: CVIU 98*, 66(2):207–222, 1997.
19. C. DeBoor. *A practical guide to splines*. Springer-Verlag, 1978.
20. J. Gee, M. Reivich, and R. Bajcsy. Elastically deforming 3d atlas to match anatomical brain images. *Journal of Computer Assisted Tomography*, 17:225–236, 1993.

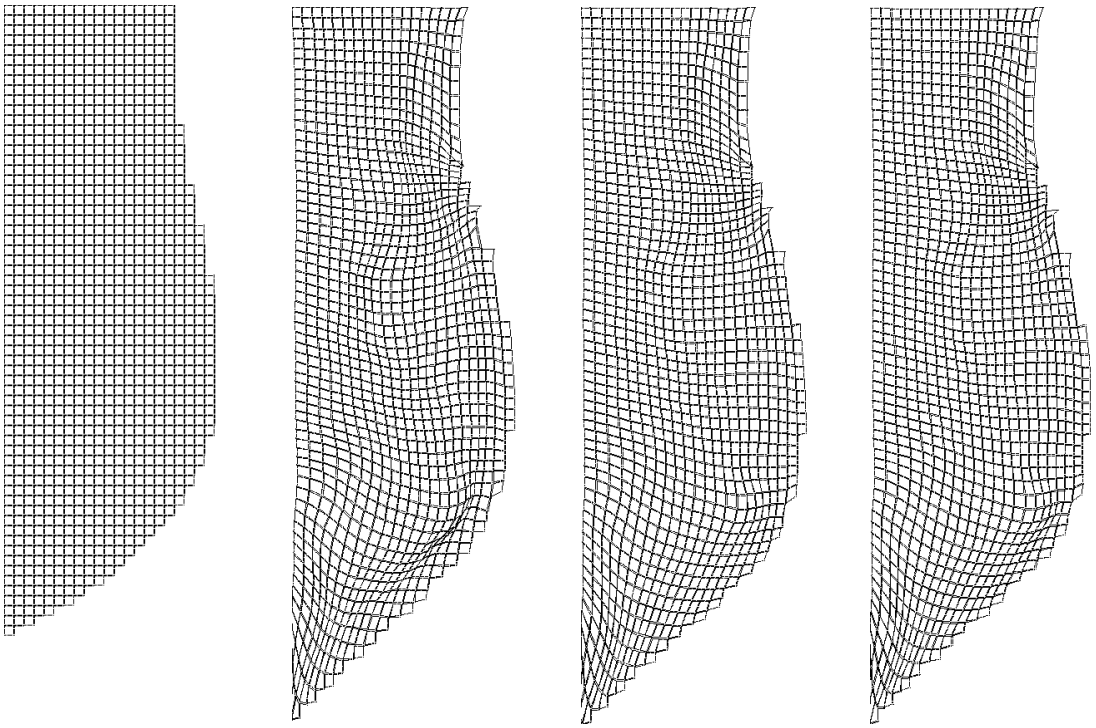

(a) (b) (c) (d)

Figure 18. Bilateral mammograms # 035/036. (a) The tessellated breast domain Ω_1 in I^1, the image $\phi(\Omega_1)$ of Ω_1 by the mapping ϕ obtained with (b) the application of model 2, (c) the application of model 3 with γ_2 equal to 0, (d) the application of model 3 with γ_2 equal to 1000.

21. M.L. Giger. Current issues in CAD. In K. Doi et al., editors, *Proc. of the 3rd International Workshop on Digital Mammography*, pages 53–60, Chicago, June 1996. Elsevier Science.
22. U. Grenander and M.I. Miller. Computational Anatomy: an emerging discipline. *Quarterly of Applied Mathematics*, 56(4):617–694, December 1998.
23. W. Hand, J.L. Semmlow, L.V. Ackerman, and F.S Alcorn. Computer screening of Xeromammograms: a technique for defining suspicious areas of the breast. *Computers and Biomedical Research*, 12:445–460, 1979.
24. R.P. Highnam, J. M. Brady, and B. J. Shepstone. A representation for mammographic image processing. In *Proc. of the First International Conference on Computer Vision, Virtual Reality and Robotics in Medicine*, Nice, France, 1995.
25. R.P. Highnam and J.M. Brady. *Mammographic image analysis*. Kluwer series in Medical Imaging. Kluwer Academic Publishers, Dordrecht; Boston, March 1999.
26. R.P. Highnam, J.M. Brady, and B.J. Shepstone. A quantitative feature to aid diagnosis in mammography. In K. Doi et al., editors, *Proc. of the 3rd International Workshop on Digital Mammography*, pages 201–206, Chicago, June 1996. Elsevier Science.
27. R.P. Highnam, J.M. Brady, and B.J. Shepstone. Estimating compressed breast thickness. In *Proc. of the 4th International Workshop on Digital Mammography*, Nijmegen, The Netherlands, June 1998.

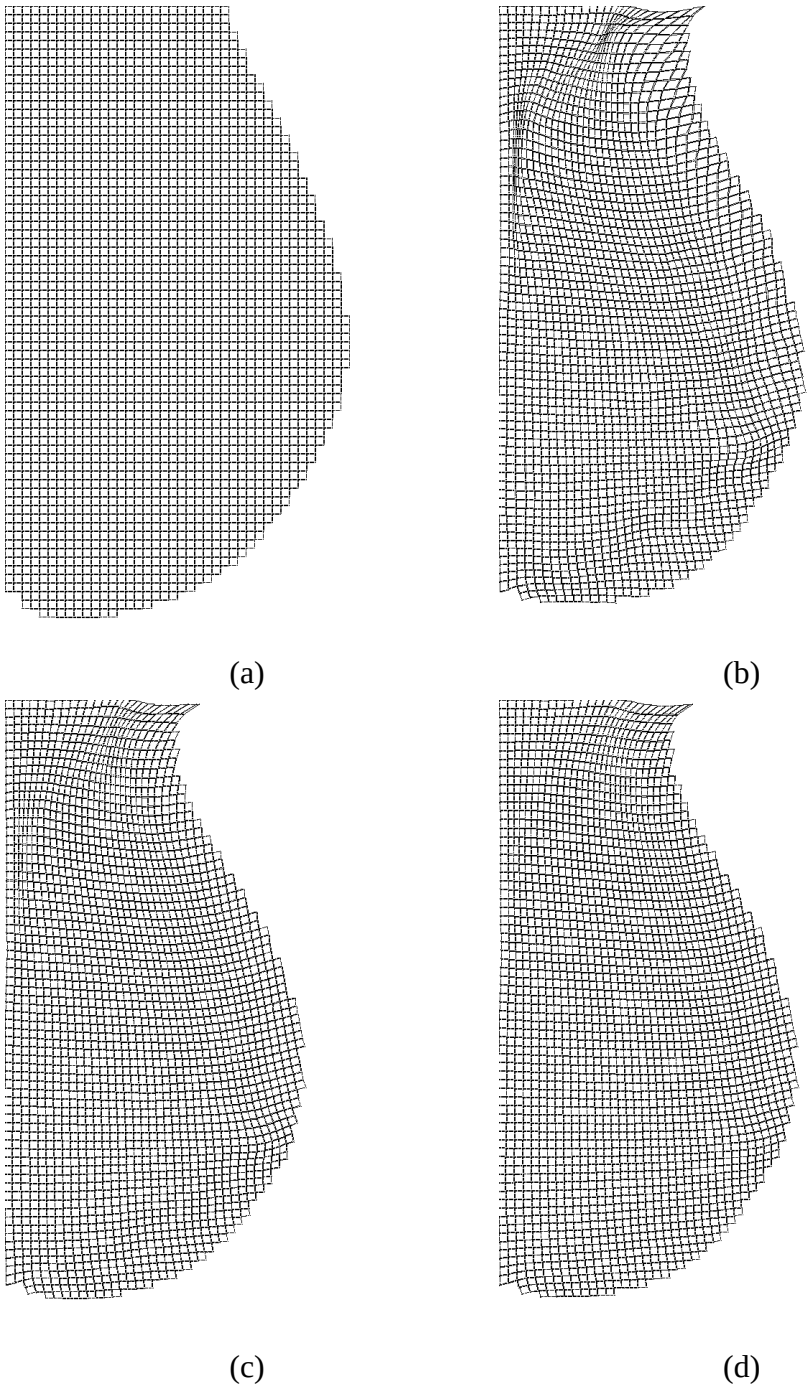

Figure 19. Bilateral mammograms # 077/078. (a) The tessellated breast domain Ω_1 in I^1, the image $\phi(\Omega_1)$ of Ω_1 by the mapping ϕ obtained with (b) the application of model 2, (c) the application of model 3 with γ_2 equal to 0, (d) the application of model 3 with γ_2 equal to 1000.

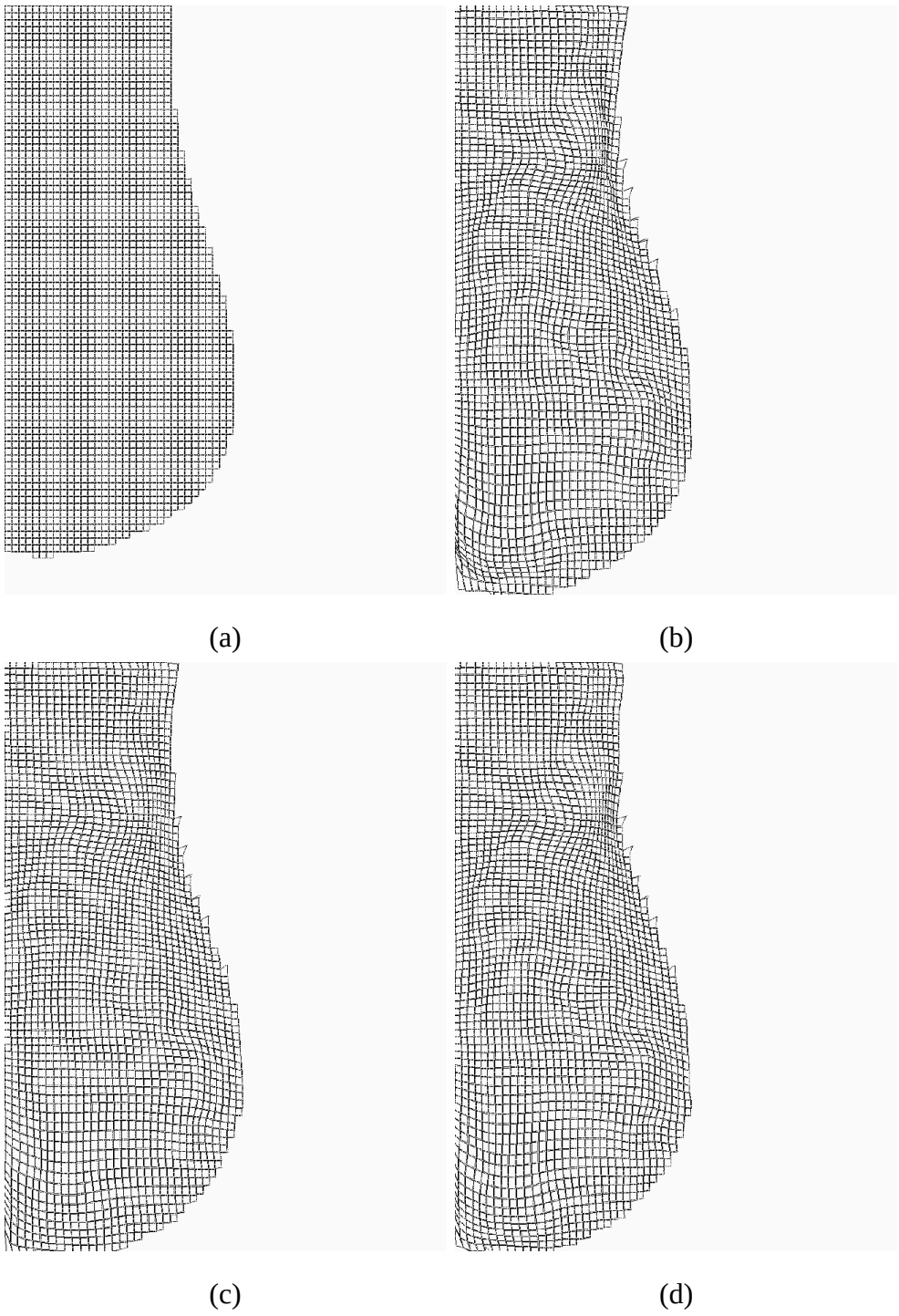

Figure 20. Bilateral mammograms # 047/048. (a) The tessellated breast domain Ω_1 in I^1, the image $\phi(\Omega_1)$ of Ω_1 by the mapping ϕ obtained with (b) the application of model 2, (c) the application of model 3 with γ_2 equal to 0, (d) the application of model 3 with γ_2 equal to 1000.

28. N. Karssemeijer. Recognition of stellate lesions in digital mammograms. In A.G. Gale et al., editors, *Proc. of the 2nd International Workshop on Digital Mammography*, pages 211–219, York, England, July 1994. Elsevier Science.
29. N. Karssemeijer and G.M. te Brake. Combining single view features and asymmetry for detection of mass lesions. In N. Karssemeijer et al., editors, *Proc. of the 4th International Workshop on Digital Mammography*, pages 95–102, Nijmegen, The Netherlands, June 1998. Kluwer Academic.
30. M. Kass, A. Witkin, and D. Terzopoulos. Snakes: Active Contour Models. *International Journal of Computer Vision*, 1(4):321–331, 1988.
31. C. Kimme, B.J. O'Loughlin, and J. Sklansky. Automatic detection of suspicious abnormalities in breast radiographs. In A. Kinger et al., editors, *Data Structures, Computer Graphics and Pattern Recognition*, pages 427–447. Academic Press, New York, 1975.
32. Y. Kita, R. P. Highnam, and J. M. Brady. Correspondence between two different views of x-ray mammograms using simulation of breast deformation. In *Computer Vision and Pattern Recognition Conference (CVPR)*, Santa Barbara, California, USA, June 1998. Computer Society Press.
33. S.L. Kok-Wiles. *Comparing Mammogram Pairs in the Detection of Mammographic Lesions*. PhD Dissertation, University of Oxford, Department of Engineering Science, 1998.
34. S.L. Kok-Wiles, J.M. Brady, and R.P. Highnam. Comparing mammogram pairs in the detection of lesions. In *Proc. of the 4th International Workshop on Digital Mammography*, Nijmegen, The Netherlands, June 1998.
35. S.L. Kok-Wiles, J.M. Brady, and A. Noble. Modelling essential breast tissue and its application to mammogram sequence analysis. In *Proc. of the 2nd Asian Conference on Computer Vision*, December 1995.
36. T.K. Lau and W.F. Bischof. Automated detection of breast tumors using the asymmetry approach. *Computers and Biomedical Research*, 24(3):273–295, 1991.
37. M. Lefébure and L. D. Cohen. Image registration, optical flow and local rigidity. *Journal of Mathematical Imaging and Vision*, 14(2), mar 2001.
38. J. Maintz and M.A. Viergever. A survey of medical image registration. *Medical Image Analysis*, 2(1):1–36, 1998.
39. K. Marias and J.M. Brady. Multi-scale landmark selection for improved registration of temporal mammograms. In M. Yaffe, editor, *Proc. of the 5th International Workshop on Digital Mammography*, pages 580–586, Toronto, Canada, June 2000. Medical Physics Publishing.
40. K. Marias, J.M. Brady, S. Parbhoo, et al. Registration and matching of temporal mammograms detecting abnormalities. In *MIUA*, Oxford, England, 1999.
41. R. Marti, R. Zwiggelaar, and C.M.E. Rubin. Automatic point correspondence and registration based on linear structures. *International Journal of Pattern Recognition and Artificial Intelligence*, 16(3):331–340, 2002.
42. P. Miller and S. Astley. Automated detection of breast asymmetry using anatomical features. In K. W. Bowyer and S. Astley, editors, *State of the Art in Digital Mammographic Image Analysis*, Series in Machine Perception and Artificial Intelligence vol. 9, pages 247–261. World Scientific, 1994.
43. R. Novak. *Transformation of the female breast during compression at mammography with special reference to importance for localization of a lesion.* PhD thesis, Departement of Diagnostic Radiology at Lakarhuset and Karolinska Sjukhuset, Sweden, 1989.

44. R. Rabbitt, J. Weiss, G. Christensen, et al. Mapping of hyperelastic deformable templates using the finite element method. In *Proc. of SPIE*, volume 2573 of *International Symposium on Optical Science, Engineering, and Instrumentation*, pages 252–265, San Diego, CA, USA, July 1995.
45. F. Richard. *Modèles élastiques d'ajustements d'images et applications aux paires bilatérales et temporelles de mammographies*. PhD thesis, University Paris 5, France, dec 2000.
46. F. Richard and L. D. Cohen. A new image registration technique with free boundary constraints: application to mammography. In A. Heyden et al., editor, *Proc. European Conference on Computer Vision (ECCV)*, volume 4, pages 531–545, Copenhaguen, Denmark, may 2002. Springer.
47. F. Richard and C. Graffigne. An image-matching model for the registration of temporal or bilateral mammogram pairs. In M. Yaffe, editor, *IWDM*, pages 756–762, Toronto, Canada, June 2000. Medical Physics.
48. M. Sallam and K. Bowyer. Detecting abnormal densities in mammograms by comparison to previous screenings. In K. Doi et al., editors, *Proc. of the 3rd International Workshop on Digital Mammography*, pages 417–420, Chicago, June 1996. Elsevier Science.
49. M.Y. Sallam. *Image unwraping and difference analysis: A technique for detecting abnormalities in mammograms*. PhD Dissertation, University of South Florida, Department of Computer Science and Engineering, April 1997.
50. M.Y. Sallam and K. Bowyer. Registering time sequences of mammograms using a two-dimensional image unwarping technique. In A.G. Gale et al., editors, *Proc. of the 2nd International Workshop on Digital Mammography*, pages 121–130, York, England, July 1994. Elsevier Science.
51. M.Y. Sallam and K. Bowyer. Registering time sequences of mammograms using a two-dimensional image unwarping technique. In A.G. Gale et al., editors, *Proc. of the 2nd International Workshop on Digital Mammography*, pages 121–130, York, England, July 1994. Elsevier Science.
52. M.Y. Sallam and K. Bowyer. Registration and difference analysis of corresponding mammogram images. *Medical Image Analysis*, 3(2):103–118, 1999.
53. J.L. Semmlow, A. Shadagopappan, L.V. Ackerman, et al. A fully automated system for screening Xeromammograms. *Computers and Biomedical Research*, 13:350–362, 1980.
54. A. Stamatakis, A.Y. Cairns, I.W. Ricketts, et al. A novel approach to aligning mammograms. In A. Gale et al., editors, *Proc. of the 2nd International Workshop on Digital Mammography*, pages 355–364, England, jul 1994. Elsevier Science.
55. J. Suckling, J. Parker, D.R. Dance, et al. The Mammographic Image Analysis Society digital mammogram database. In A.G. Gale et al., editors, *Proc. of the 2nd International Workshop on Digital Mammography*, York, England, July 1994.
56. L. Tabár and P. Dean. *Teaching atlas of mammography*. Thieme Inc., Stuttgart, 1985.
57. A. Toga. *Brain mapping*. Academic Press, 1999.
58. B. Vemuri, Y. Chen, and Z. Wang. Registration assisted image smoothing and segmentation. In A. Heyden et al., editor, *Proc. European Conference on Computer Vision (ECCV)*, volume 3, pages 546–559, Copenhaguen, Denmark, may 2002. Springer.
59. N. Vujovic. *Registration of Time-Sequences of Random Textures with Application to Mammogram Follow-up*. PhD thesis, Lehigh University, 1997.

60. N. Vujović, P. Bakić, and D. Brzaković. Detection of potentially cancerous signs by mammogram followup. In K. Doi et al., editors, *Proc. of the 3rd International Workshop on Digital Mammography*, pages 421–424, Chicago, June 1996. Elsevier Science.
61. N. Vujović and D. Brzaković. Control points in pairs of mammographic images. *IEEE IP*, 6(10):1388–1399, October 1997.
62. C.J. Vyborny and M.L. Giger. Computer Vision and Artificial Intelligence in Mammography. *American Journal of Roentgenology*, 162:699–708, 1994.
63. F. Winsberg, M. Elkin, J. Macy, et al. Detection of radiographic abnormalities in mammograms by means of optical scanning and computer analysis. *Radiology*, 89:211–215, August 1967.
64. A. Witkin, T. Terzopoulos, and M. Kass. Signal matching through scale space. *International Journal of Computer Vision*, 1(2):133–144, 1987.
65. A. Yezzi, L. Zöllei, and T. Kapur. A variational framework for joint segmentation and registration. In *IEEE Workshop on Biomedical Image Analysis (WBIA)*, pages 44–51, Kauai, Hawaii, 2001.
66. F.-F. Yin, M.L. Giger, K. Doi, et al. Computerized detection of masses in digital mammograms: Automated alignement of breast images and its effect on bilateral-substraction technique. *Medical Physics*, 21(3):445–452, March 1994.
67. F.-F. Yin, M.L. Giger, C.J. Vyborny, et al. Comparison of bilateral substraction and single-image processing techniques in computerized detection of mammographic masses. *Investigate Radiology*, 28(6):473–481, 1993.
68. X. Zhou and R. Gordan. Geometric unwarping for digital substraction mammography. In *Proc. of Vision Interface (VI)*, pages 25–30, Edmonton, Alberta, Canada, 1988.